School of Industrial and Information Engineering

Master of Science in Materials Engineering and Nanotechnology

Department of Chemistry, Materials and Chemical Engineering "G. Natta"

POLITECNICO
MILANO 1863

Hybrid Modification of Epoxy Resin with Micro-Fibrillated Cellulose and Rubber Nanoparticle: Effects on the Mechanical Properties of Carbon Plain-Weave Reinforced Composites

Supervisor: Prof. Valter Carvelli

Co-Supervisor: Prof. Toru Fujii

Master Thesis of:

Andrea Betti

Matr: 782338

Academic Year 2014-2015

"Whenever the essential nature of things is analyzed by the intellect, it must seem absurd or paradoxical. This has always been recognized by the mystics, but has become a problem in science only very recently."

F. Capra 1975

Contents

List of Tables

List of Figures

Abstract

This work details an experimental investigation on understanding the effects of hybrid epoxy resins, filled with micro-fibrillated cellulose (MFC) and carboxylated nitrile butadiene rubber (XNBR), on the principal mechanical properties of carbon plain weave textile reinforced composites. Twelve combinations of MFC and XNBR weight contents in the epoxy resin (from 0 to 0.5 wt% MFC and from 0 to 3 wt% XNBR) were considered for quasi-static tensile, short beam and impact tests. Moreover, five of the twelve materials were selected to study the tensile-tensile fatigue behavior considering different loading levels. The investigation revealed that the inter-laminar shear strength (ILSS) increased more than 32% for 0.1 wt% MFC and 3 wt% XNBR, while the tensile strength increased 10% for 0.3 wt% MFC and 3 wt% XNBR. Furthermore, the experimental results show that the best impact and fatigue performance, for the considered weight contents of fillers, is of the composite enhanced with the maximum content of MFC. The SEM observations of the fracture surfaces indicate the extensive "plastic" deformation of the matrix and the improved fiber-matrix adhesion with increase of the MFC and XNBR contents.

Estratto in Italiano

Lo studio descrive i risultati di un lavoro sperimentale atto a comprendere l'effetto di matrici epossidiche ibride, caricate con cellulosa micro fibrillata (MFC) e gomma nitrilica carbossilata (XNBR), sulle principale caratteristiche meccaniche di compositi rinforzati con tessuto in fibra di carbonio. Dodici combinazioni di MFC e XNBR nella resina epossidica (da 0 a 0.5 wt% MFC e da 0 a 3 wt% XNBR) sono state considerate per test statici di trazione, resistenza interlaminare e di impatto. Inoltre, cinque combinazioni delle dodici sono state selezionate per studiare il comportamento a fatica considerando diversi livelli di carico. I risultati hanno evidenziato un incremento nella resistenza a taglio interlaminare (ILSS) di oltre il 32% per il contenuto di 0.1 wt% MFC e 3 wt% XNBR, mentre il carico di rottura a trazione ha registrato un incremento del 10% per lo 0.3 wt% di MFC e 3 wt% di XNBR. Infine i risultati sperimentali hanno mostrato che il materiale con le migliori caratteristiche a impatto e fatica, per i contenuti analizzati, è quello realizzato con la resina contenente il massimo contenuto di MFC. Le osservazioni con il SEM hanno evidenziato una deformazione "plastica" della matrice e un incremento della resistenza dell'interfaccia fibra-matrice all'aumentare del contenuto di MFC e XNBR nella resina epossidica.

Chapter 1

Introduction

1.1 Overview

The Present work was performed at Doshisha University in Kyoto, Japan in the Department of Mechanical Engineering and Systems (Advanced Material and Structural Engineering Laboratory, AMSEL) and at Politecnico di Milano. It was a two-year project partially founded by JSPS KAKENHI (grant Number 26289012).

The project gives a contribution to understand the effects of hybrid epoxy resins, filled with twelve different combinations of micro-fibrillated cellulose (MFC) and carboxylated nirile butadiene rubber (XNBR), on the mechanical properties of carbon plain weave textile composites. The adopted hybrid epoxy system intends to couple the effects of both fillers. Namely, the improvement of interfacial adhesion observed with MFC and the resin ductility attributed to the rubber nanoparticles.

1.1.1 Work Organization

The main research goals of the present master thesis are:

1. Resin hybridization and composite manufacturing, preparation of laminate sheets and production of cupons for testing;

2. Experimental investigation of the mechanical properties of the materials focusing on:

   (a) Quasi-static tensile properties;

   (b) Inter-laminar strength;

   (c) Impact resilience;

   (d) Tensile-tensile fatigue behavior of the best performing combination of MFC and XNBR.

3. Observation of the macro and microscopic damage evolution mechanism occurring in the composite laminate during static and dynamic loading exploiting the following techniques:

   (a) Scanning electron microscope observation;

   (b) Digital image correlation measurements;

   (c) Temperature mapping of the specimens.

The dissertation will be organized in five sections as summarized in Table 1.1.

Chapter	Content
1 Introduction	
2 Materials and manufacturing	Properties of components Composite preparation Specimens preparation
3 Experimental devices and Setups	Quasi-static tensile tests Short beam tests Impact tests Tensile fatigue tests Digital image correlation Thermal camera Optical microscope Scanning electron microscope
4 Results and discussion	Quasi-static tensile tests Short beam tests Impact tests Tensile fatigue tests
5 Conclusions and future developments	

Table 1.1: Organization of work.

1.2 Literature Review

1.2.1 Composite Materials

A composite material is defined as a "two or more materials or phases used together to give a combination of properties that cannot be attained otherwise" [1].

It is possible to distinguish many classes of composite materials, but there is a common aspect which represents the main difference with respect to the other engineering materials: a composite material is designed at the same time as the product. Fiber and resin type, proportions of each constituent and stacking sequence are selected in order to obtain the best properties for that specific application [2].

Thanks to this extreme flexibility, composite materials, if properly used, offer many advantages over metals: some examples are high strength and high stiffness-to-weight ratio, corrosion resistance and low thermal expansion. On the other hand, conventional composites also have some disadvantages, such as poor transverse properties, inability to yield and sensitivity to moisture and high temperatures; all these drawbacks should properly be accounted in the design phase.

In Table 1.2 the main mechanical properties of composite quasi-isotropic laminates are compared to the traditional structural materials. It is clearly visible that the strength-to-weight ratio and the modulus-to-weight ratio are much higher than aluminum or steel.

These extraordinary mechanical properties make composite materials attractive to several industrial applications [3]. The driving force of this trend is the weight reduction, aimed at avoiding excessive emissions, in addition to excellent chemical and corrosion resistance, high dimensional stability and

Material	**Fiber Content** [% Vol]	**Modulus** E [GPa]	**Tensile Strength** σ_u [MPa]	**Density** ρ [g/cm^3]
Steel		210	450 ÷ 830	7.8
Aluminum 2024-T4		73	410	2.7
Aluminum 6061-T6		69	260	2.7
E-glass/Epoxy	57	21.5	570	1.97
Kevlar 49/Epoxy	60	40	650	1.4
Graphite/Epoxy	58	83	380	1.54
Boron/Epoxy	60	106	380	2

Table 1.2: Comparison between mechanical properties of traditional materials and composites. These values are valid for quasi-isotropic composite laminates.

viscoelastic properties.

One of the most extensive applications of composite materials for structural purpose is in the aerospace and aircraft industry, where it is absolutely necessary to improve the efficiency and performance of the aircraft in order to considerably reduce the development and operating costs. An important contribution can be achieved by decreasing the aircraft weight through considerable usage of composite materials in primary aircraft structures.

An evident example of aircraft structures where composite materials play a fundamental role is given by Boeing 787, which makes greater use of composite materials in its airframe and primary structure than any previous Boeing commercial airplane. The result is an airframe comprising of nearly half carbon fiber reinforced plastic and other composites. This approach offers weight saving of an average 20% compared to conventional aluminum design (Fig. 1.1) [4]. Composites are used on the fuselage, wings, tail, doors and interiors.

The extensive use of composite, especially in the highly tension-loaded environment of the fuselage, greatly reduces the maintenance due to fatigue,

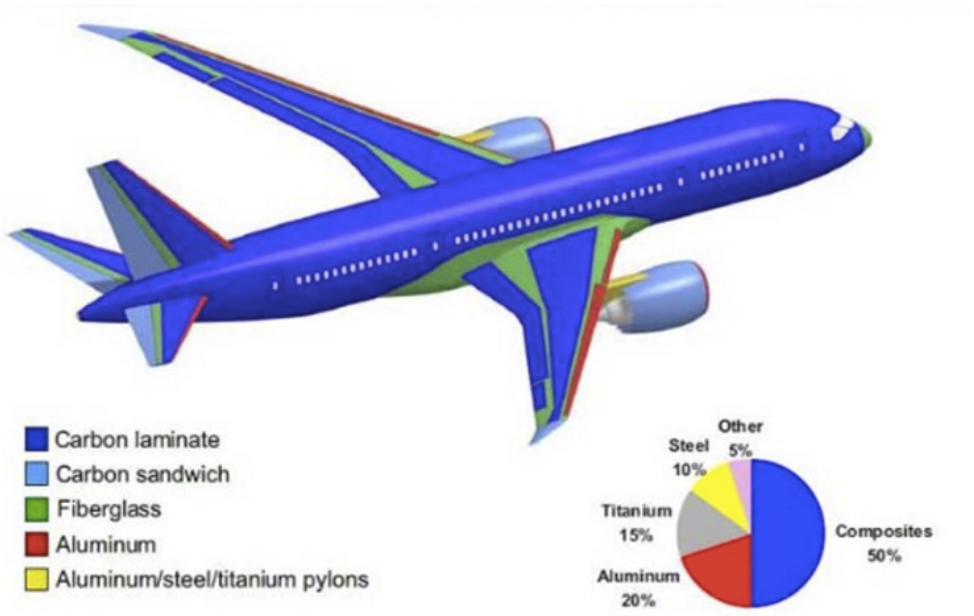

Figure 1.1: Materials used in Boeing 787. Reproduced from [4].

when compared to aluminum structures. This type of analysis has resulted in an increased use of titanium as well. Where loading indicates that metal is the preferred material system, but environmental considerations indicate aluminum is a poor choice, titanium is an excellent low-maintenance design solution. In addition to lowering the overall airplane weight, moving to a composite structure provides the opportunity to reduce both the scheduled and non-routine maintenance burden on the airlines, since composite structures require less maintenance than conventional structures.

As a consequence of the above statements, it is possible to understand why, over the past decades, industries have put a lot of effort to enhance the mechanical performance of composite materials.

1.2.2 Matrix Toughening

Research efforts were dedicated to the development of toughened fiber-matrix composites, with basically two distinct approaches [5]. The first approach is based on 3D fiber reinforcement using advanced textile techniques [6], e.g. stitching, z-pinning, weaving, braiding, knitting, etc.. It could not be an effective way to fabricate toughened composites, the reduction of the in-plane effective fiber volume fraction and local damage imparted in manufacturing (e.g. stitching) could lead to a decrease of in-plane stiffness and strength [7]. But efficient modern technologies of low-cost manufacturing of 3D single-layer performs can improve the damage tolerance and the mechanical performance of composites ([8] and [9]).

The second approach is to develop modified epoxy resins with improved toughness. Modified thermosetting matrix resins for reinforced composites have evolved greatly over the past three decades in overcoming the brittle nature of thermosetting polymers by dispersion of a second phase that normally consist of nano- or micro-sized fillers. Different fillers are known to increase the mechanical property of the epoxy matrix such as carbon nanotubes, nano-fibers, nano-particles and rubber (see e.g. [10], [11], [12], [13] and [14]). Fillers are expected to provide extrinsic toughening mechanism [15] and, as a consequence, to positively affect the mechanical response of fiber reinforced composite materials. In the large range of micro and nano fillers adopted in thermoset matrices hybridization, two were selected in this thesis: Micro-Fibrillated Cellulose and Rubber Nanoporticle.

1.2.3 Micro-Fibrillated Cellulose

The identification of nano-sized cellulose microfibrils, named micro-fibrillated cellulose (MFC) [16], increased the family of hybrid nano-enhanced composite materials [17]. Cellulose is the most abundant natural homo-polymer and one of the most promising renewable and environmentally friendly resources [18]. MFC were first produced in 1983 by Herrick [19] and Turbak [16] using wood pulp and a high pressure homogenizer which promoted the disintegration of cellulosic fibers into sub-structural fibrils and microfibrils having lengths in the micro-scale, width ranging from 10 to a few hundred nanometers and a web-like structure (Fig. 1.2).

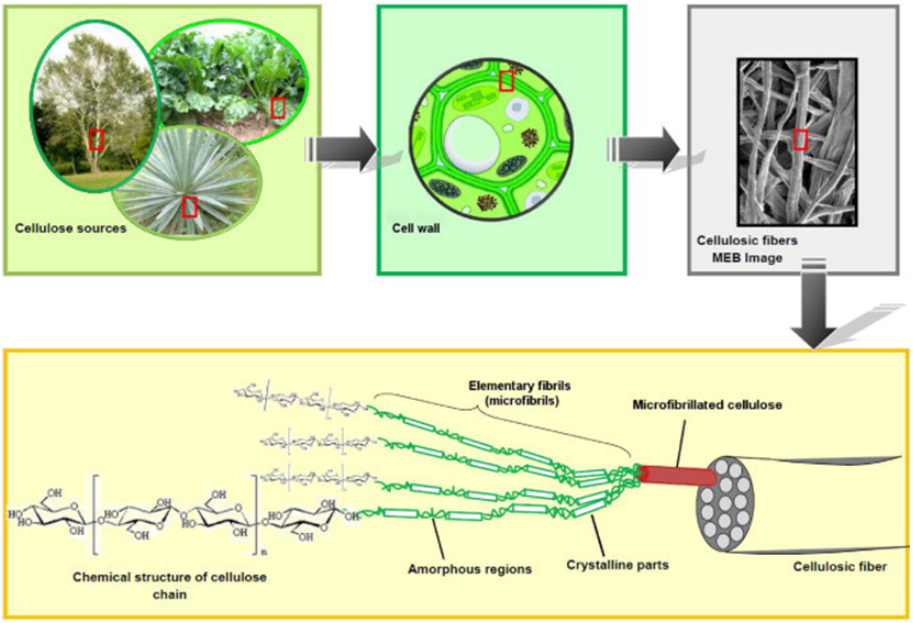

Figure 1.2: From cellulose sources to cellulose molecules: details of the fiber structure with emphasis on the cellulose microfibrils (in color). [20].

MFC can be produced from various sources, such as wood and non-wood fibers, bacterial, and animal-derived cellulose. MFC are typically produced by four mechanical methods: homogenization, micro-fluidization,

micro-grinding, and cryo-crushing. Homogenization is most commonly utilized in food and paint processing, particularly to produce homogenized milk and to disperse dyes and pigments in paints. When processing with a homogenizer, cellulose fibers are passed through either one or two stages, where the fibers are subjected to rapid pressure drops, high shear, and impact forces against a valve and an impact ring. The pressure drop is typically around 55 MPa and the fibers are cycled through the homogenizer approximately $10 \div 20$ times. Overall, it can be stated that homogenization is an energy-intensive process. Beside the large energy consumption, a main disadvantage of the homogenization is that long fibers often clog the system [20]. However, the homogenizer can be easily scaled to industrial production and can be operated as continuous process.

Plant derived cellulose were adopted as either composite reinforcement [18], or biodegradable natural polymer matrix [17], and even as all cellulose composites [21]. The effect on the tensile mechanical properties and fracture toughness of micro-fibrillated cellulose-based epoxy reinforced carbon plain woven was investigated by Gabr et al. [22]. Results in [22] reveal a major role of MFC to improve the inter-laminar fracture toughness in mode I, which could be attribute to strong adhesion between filled epoxy and carbon fibers. The mentioned and other results available in literature show the important improvement of the damage tolerance of composite materials enhanced with the proper content of MFC for quasi-static loading.

1.2.4 Rubber Nanoparticle

Several studies involved the chemical modification of epoxy resins with reactive liquid rubber, particularly carboxyl-terminated butadiene acrylonitrile (CTBN), see e.g. [23]. The micro-structure consists of an elastomeric

phase dispersed in the epoxy matrix with the elastomeric particle diameter of hundreds of nanometers. It is attributed to the rubber nano-particles the formation of a plastic shear yielding zone near the crack tip, producing blunting of the crack, bringing about the reduction of stress concentration near the crack tip which consequently improves the fracture toughness [24]. Furthermore, the addition of rubber nano-sized particles leads to an improvement of fatigue performance for both pure epoxy resin ([25], [26] and [27]) and carbon fiber reinforced composites [28].

The hydrostatic tension causes rapid cavitation of the rubber and growth of the resultant voids. This voided zone blunts the crack, causing it to behave as if it had a larger crack-tip radius. This blunt crack, upon the application of further tension, causes an even larger plastic zone to form. Thus, a large volume of material above and below the crack plane is caused to undergo plastic deformation. The creation of this plastic zone is the principal toughening mechanism (Fig. 1.3) [29].

Epoxy matrix modified with micro-fibrillated cellulose and carboxyl-terminated butadiene acrylonitrile as liquid rubber was adopted to improve the interfacial adhesion in plain woven carbon fiber composites in [30]. The hybrid epoxy resin increased the inter-laminar fracture toughness in mode I as discussed in [31].

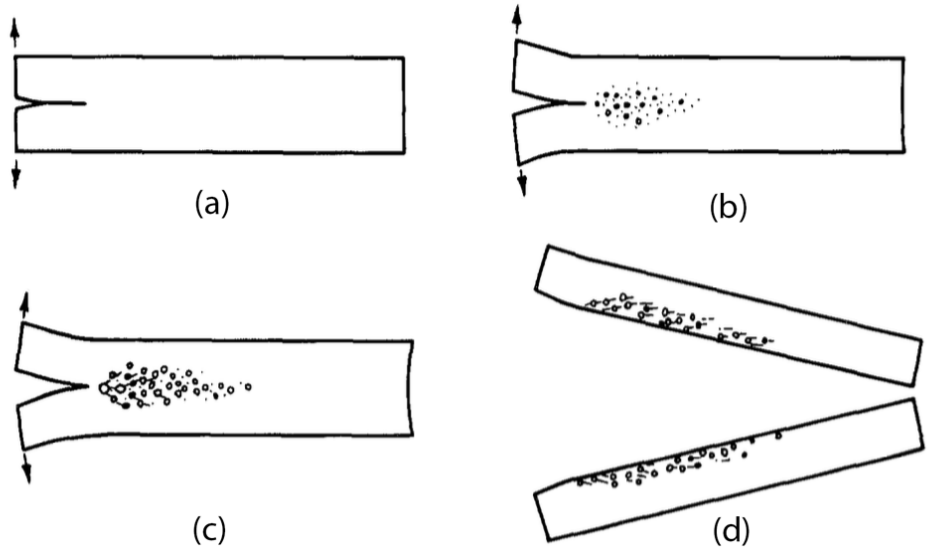

Figure 1.3: A schematic representation of the deformation processes ahead of a crack tip. (a) A crack is subjected to a load in the opening mode; (b) increasing displacement and load causes the rubber particles in a zone ahead of the crack tip to cavitate; (c) on further loading, cavities grow larger, with those at highest stress levels initiating shear bands; (d) finally, if the strain energy continues to increase, the critical level is reached and unstable (fast) fracture occurs. [29].

Chapter 2

Materials and Manufacturing

2.1 Properties of Components

In this section all the components used for the fabrication of the composite are detailed. The components with their own supplier are shown in Table 2.1.

	Supplier	**Grade**
Epoxy Resin	Mitsubishi Co. Ltd.	jER^{TM} 828
Carbon Fiber	Mitsubishi Rayon Co. Ltd.	Pyrofil^{TM} TR3110M
MFC	Daicel Chemical Industries Ltd.	Celish^{TM} KY100G
XNBR	JSR Corporation Ltd.	XNBR N202S

Table 2.1: List of components suppliers and grades.

2.1.1 Epoxy Resin

The epoxy resins are thermosetting polymers that contain at least two epoxide groups. The thermosetting process is usually referred as curing. While curing, the polymer undergoes a cross-linking reaction that is triggered

by the mixing with the so called curing agent. Epoxy resins are widely spread in composite industry because of their mechanical and chemical resistance properties; moreover the processing of epoxy resins is rather simple which allows easy manufacturing process such as hand lay-up.

In this work a general grade bisphenol A liquid epoxy resin was used (jER^{TM} 828, Fig. 2.1) whose main properties are shown in Table 2.2. As curing agent a modified cycloaliphatic amine was adopted (jERCURE^{TM} 113) which shows good stability for heating casting and is made for specific application on laminate parts [32]. Both the resin and the curing agent were provided by Mitsubishi Co. Ltd.

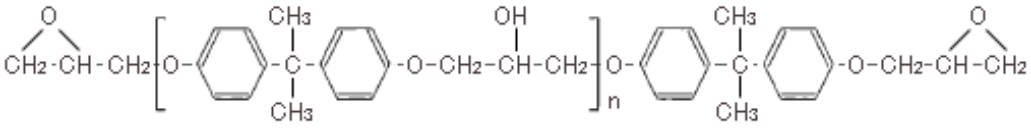

Figure 2.1: Chemical Structure of jER^{TM} Epoxy Resin [33].

Viscosity η [poise @ 25 °C]	**Molecular Weight** M_w [g/mol]
120 ÷ 150	≈370

Table 2.2: Properties of Grade 828 Epoxy Resin jER^{TM} [34].

2.1.2 Carbon Textile Reinforcement

The reinforcement adopted in this work was a balanced carbon fibers plain weave textile (Pyrofil^{TM} TR3110M) provided by Mitsubishi Rayon Co. Ltd., Japan. The main properties of woven fabric and single tow are shown in Tables 2.3 and 2.4 respectively. Carbon fiber is a light and tough material made from polyacrylonitrile (PAN) fiber carbonized at high temperatures

Style	**Yarn**		**Count**[ends/cm]		**Weight**	**Thickness**
	Warp	Fill	Ends	Picks	[g/m^2]	[mm]
Plain	TR30S3L	TR30S3L	4.87	4.87	200	0.23

Table 2.3: Properties of woven fabric [35].

Filaments	**Fiber Diameter** ϕ [µm]	**Linear Density** [TEX]	**Ultimate Strain** σ_u [MPa]	**Modulus** M [GPa]	**Elongation** ε_u [%]	**Density** ρ [g/cm^3]
3000	7	200	4120	234	1.8	1.79

Table 2.4: Physical and mechanical property of TR30S3L tow [36].

and which has a strength superior to conventional metal materials; it can be widely used in various segments such as automotive, wind energy, fuel cell as well as aerospace, sporting goods and general industrial applications. The woven textile reinforcement is selected to have an important influence of the matrix on the mechanical behavior of the composites with a higher fibers and matrix adhesion surface than for a unidirectional reinforcement.

2.1.3 Micro-Fibrillated Cellulose

The Micro-Fibrillated Cellulose is a material composed by nano-sized fibrils of cellulose. Typical dimension for fibrils are listed in the Table 2.5.

The MFC can be produced from wood-based cellulose through high-pressure homogenization process involving very high shear stresses; those stresses are able to delaminate the cell walls of fibers and to liberate the nano-sized fibrils [37].

In this work the Celish^{TM} KY100G of MFC was used (Fig. 2.2a), provided by Daicel Chemical Industries Ltd. Japan. The MFC is commercially provided in water slurry containing 10 % MFC nano-fibers. Celish^{TM} is cel-

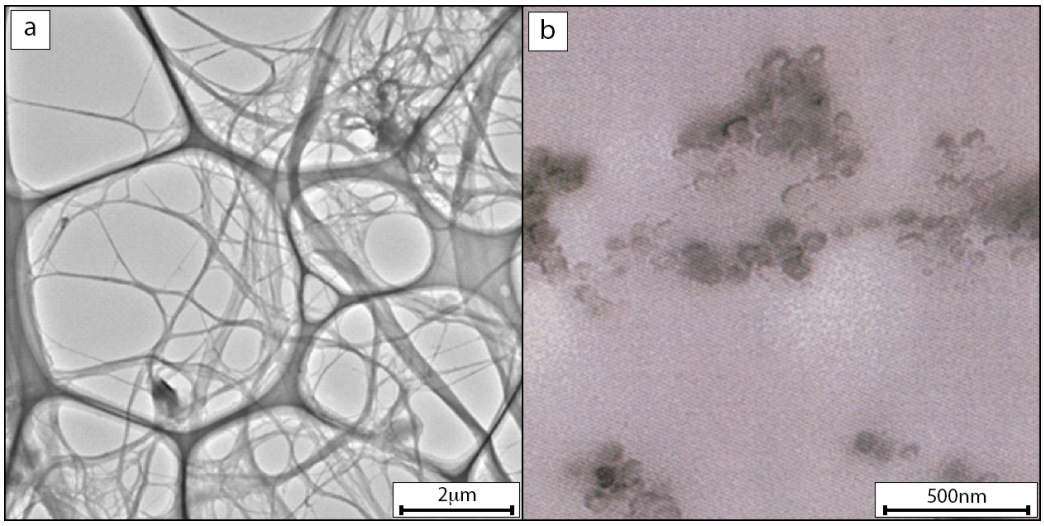

Figure 2.2: Transmission Electron Microscope (TEM) Observation of (a) MFC and (b) XNBR in epoxy matrix.

lulose nano-fiber, micro-fibrillated by special manufacturing process, and is produced from highly refined, pure fiber raw materials. The raw material fiber is unraveled into tens of thousands of strands. It is refined so that it does not impair the exact basic characteristics of the cellulose raw material (physical and chemical stability etc.) [38].

Lateral	**Longitudinal**
5 nm ÷ 20 nm	10 nm up to several mm

Table 2.5: Typical lateral and longitudinal dimensions for a single MFC fibril.

2.1.4 Rubber Nanoparticles

The rubber nanoparticles in this work are Carboxylated Nitrile Butadiene Rubber (XNBR) nanoparticles (Fig. 2.2b). Rubber was provided in bale form by JSR Corporation Ltd., Japan. After chemical dissolution, with

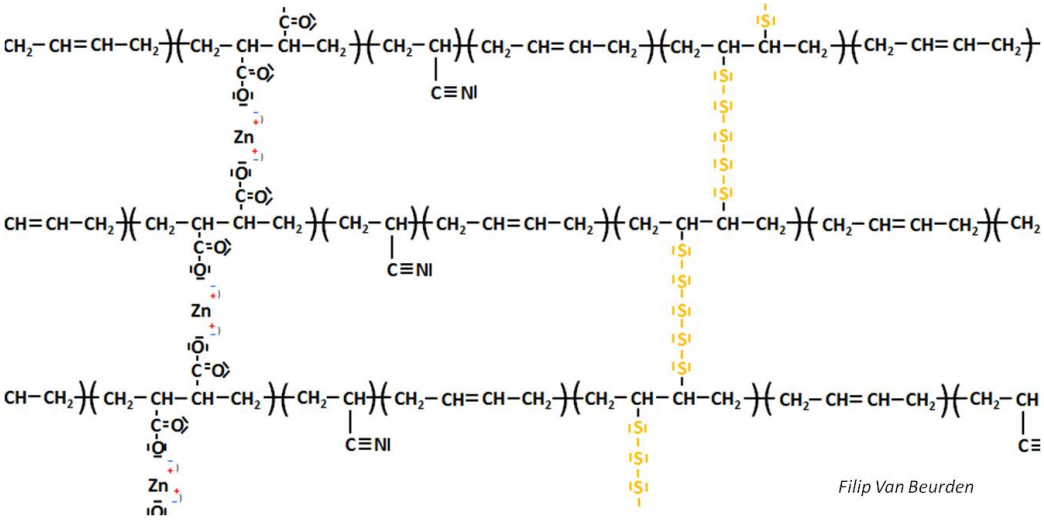

Figure 2.3: XNBR strings with a carboxyl group [39].

methyl ethyl ketone nanoparticles have a diameter in the range of 80 ÷ 200 nm. The XNBR is an improved version of Nitrile Butadiene Rubber (NBR). Although its physical and chemical properties vary depending on the polymer's composition of nitrile, this form of synthetic rubber is unusual in being generally resistant to oil, fuel, and other chemicals (Fig. 2.3). For this grade of XNBR (N202S) the main characteristics are shown in Table 2.6.

Acrilo-Nitrile Fraction AN [%]	**Tensile Strength** σ_u [MPa]	**Ultimate Strain** ε_u [%]
40	14.9	260

Table 2.6: Main physical and mechanical property of XNBR [40].

2.2 Composite Preparation

In this section it is reported the preparation of the composite, starting from the matrix modification up to manufacturing of the specimens for the

different tests.

2.2.1 Matrix Preparation

The epoxy matrix was provided in liquid form from the supplier, in a 20 kg pail.

First it was weighted, in a plastic cup, 300 g of resin, which is the correct amount for the lamination process. Then the plastic cup containing the matrix was leaved in a convection oven at 80 °C for at least 1 h; this helped to considerably decrease the viscosity of the epoxy making the further steps easier.

Once the epoxy viscosity was decreased it was possible to add the fillers.

Studied Compositions

For this work 12 different combinations of MFC and XNBR were considered. Fillers were measured as weight fraction on the total epoxy resin amount.

Four MFC contents were considered 0.0 wt%, 0.1 wt%, 0.3 wt% and 0.5 wt% assuming the results presented in [22] and [41].

Three XNBR contents were considered 0 wt%, 1 wt% and 3 wt% assuming the results presented in [24].

The different compositions were then labelled with letters from A to L according to Table 2.7.

MFC Modification

The MFC comes from provider as water slurry containing 10% of MFC fibers in weight. The first step was to dissolve the water slurry in ethanol with the ratio of 100 g of ethanol per 10 g of water slurry. Ethanol was used

	MFC			
XNBR	0.0 wt%	0.1 wt%	0.3 wt%	0.5 wt%
0 wt%	A	B	C	D
1 wt%	E	F	G	H
3 wt%	I	J	K	L

Table 2.7: Denomination of composite materials according to fillers content.

because it can substitute the water bonded to the MFC fibers, moreover it will be easier at later stage to remove the ethanol by evaporation. The mixture of MFC and ethanol was put in a process homogenizer for 15 min at 8000 rpm to obtain a good dispersion and let all the ethanol substitute the water.

After that, the mixture was filtered in a Büchner funnel to remove water and ethanol obtaining a soft sheet of MFC fibers. Then the sheet was ripped and mixed with more ethanol to completely remove all the water left. The mixture was put then in a high-speed homogenizer for 15 min at 15 000 rpm to disperse completely the fibers in the solvent.

Finally the mixture of MFC and ethanol was versed into the cup containing the epoxy. At last the cup was moved into the convection oven at 80 °C for 120 h where all the ethanol was removed by evaporation.

XNBR Modification

The XNBR comes from provider as solid bale of 35 kg, it was then necessary to dissolve in methyl ethyl ketone (MEK) to obtain the small nanoparticles.

First the rubber was cut into small pieces and weighted in a small paper cup, then was dissolved in MEK with the ratio of 100 g of solvent for 1 g

of XNBR. After that, the solution was set for 24 h on an heated magnetic stirrer running at 700 rpm; the mixture, while stirring, was heated at 80 °C in order to get a better dissolution of the rubber.

Later, the solution of XNBR in MEK was mixed with the epoxy resin that can already contain MFC and stirred using a high-speed homogenizer for 30 min at 5500 rpm.

Finally the mixture of MEK, epoxy and eventually MFC was moved into the convection oven at 80 °C for 120 h where all the MEK solvent was removed by evaporation.

2.2.2 Manufacturing Process

The manufacture process to obtain the composite laminate was the hand lay-up. The process was carried out on a heated plate at 60 °C in order to decrease the matrix viscosity and avoid air bubbles during lamination.

First the curing agent was mixed with the epoxy resin having a ratio of 32 wt%, so for 300 g of epoxy 96 g of curing agent are needed. The mixture was stirred for 5 min and after that, was degassed in a vacuum chamber for 10 min at room temperature.

After degassing the lamination process begins. An aluminum mold was used to give the desired shape and thickness to the laminate, eight plies of woven textile were cut with dimension 240×340 mm (Fig. 2.4a).

A cellophane layer was placed to facilitate the laminate removal then the matrix was distributed into the mold and the first ply was placed, between every ply some matrix was poured (Fig. 2.4b) and spread using a roller. When all plies were placed another cellophane layer was placed on the upper part of the mold. During this process attention must be devoted to the tows alignment of different layers.

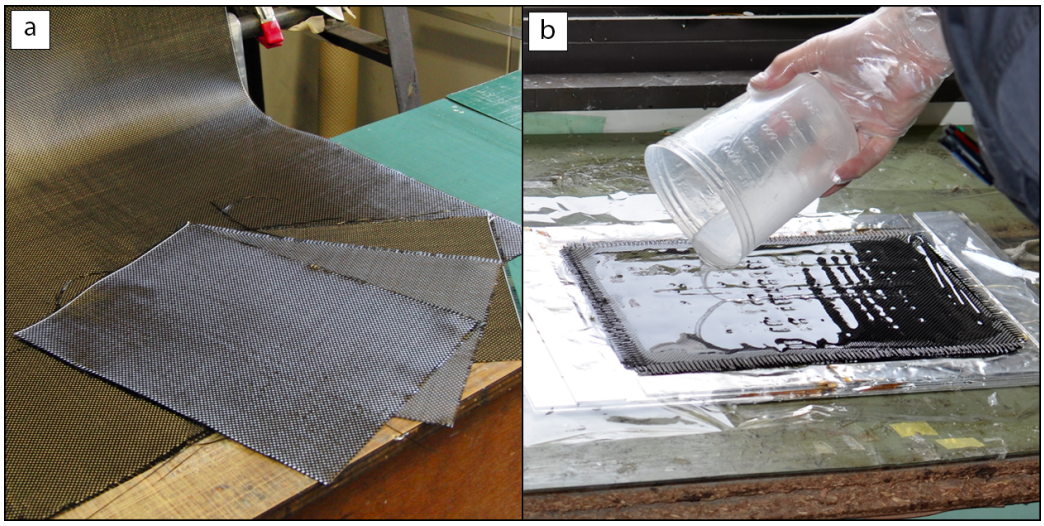

Figure 2.4: (a) Woven plies. (b) Hand lay-up process

The mold was placed in a heat press for the curing process. The curing was carried at 80 °C for 1 h and then at 150 °C for 3 h [32] keeping a constant pressure of 2 MPa (Fig. 2.5).

Finally, when curing process was over, the laminate was removed from the heat press. The resulting laminates have thickness of 1.97±0.06 mm.

2.2.3 Volume Fraction Measurements

A preliminary measurement was made to determine the actual fiber volume fraction of the composite according to the standard ISO 1172 [42]. The results were then compared with the theoretical value evaluated as follow:

$$V_f = \frac{n^{\circ}_{plies} \cdot A}{t \cdot \rho_f} \tag{2.1}$$

where, n°_{plies} is the total number of plies, A [g/mm] is the fabric areal density, t [mm] the thickness and ρ_f [g/mm^3] the fiber density. This equation gives an estimation of the volume fraction.

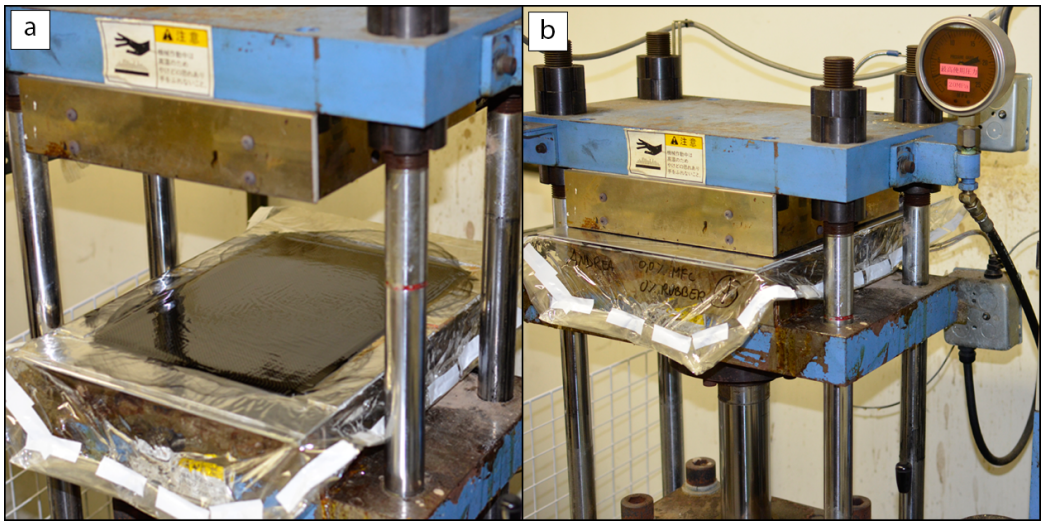

Figure 2.5: Heat press (a) before and (b) after closure.

Square specimens were prepared with dimensions of 10×10 mm and small aluminum crucibles were used. At the beginning specimens were weighted, with a scale that had resolution of 0.001 g (Infrared Moisture Determination Balance FD-720 [43]), alone and with the crucible to determine the initial weight.

The oven was set to 450 °C in order to totally burn the matrix but not so high to start the fibers degradation. The specimens were then weighted again with crucible after 2 h; then the weighings were repeated every hour until the weight of two subsequent measurements were matching.

In Table 2.8 are reported the values of fiber volume fraction according to these measurements, for each combination of fillers three specimens were tested. In total, the experimental volume fraction average is $45.66 \pm 1.87\%$ while the theoretical one is $45.67 \pm 1.64\%$.

These results confirm that even if the hand lay-up process is mostly manual and human errors may occur, it is possible to obtain repetitive results with a certain grade of accuracy.

	MFC			
XNBR	0.0 wt%	0.1 wt%	0.3 wt%	0.5 wt%
0 wt%	0.472 ± 0.005	0.460 ± 0.011	0.498 ± 0.050	0.444 ± 0.008
1 wt%	0.473 ± 0.018	0.459 ± 0.005	0.458 ± 0.008	0.441 ± 0.002
3 wt%	0.430 ± 0.005	0.434 ± 0.013	0.456 ± 0.006	0.453 ± 0.000

Table 2.8: Measured fiber volume fraction with standard deviation for the twelve different combinations of fillers.

2.3 Specimens Preparation

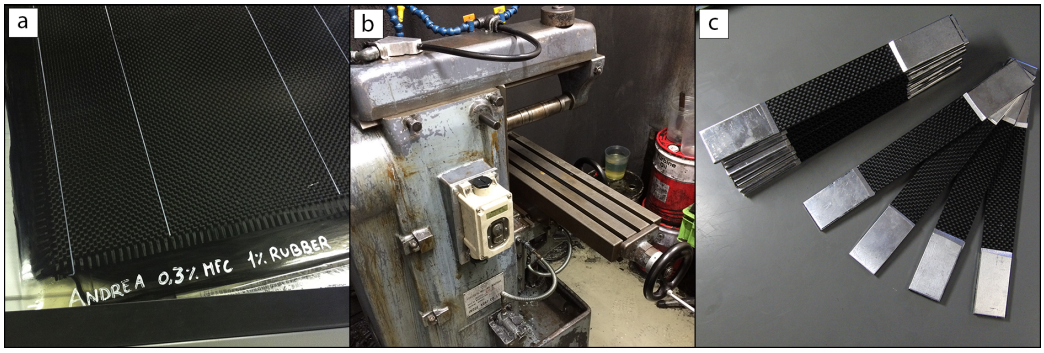

Figure 2.6: (a) Composite laminate sheet, (b) Diamond milling machine and (c) Specimens for quasi-static tensile and tensile fatigue tests with tabs.

After the manufacturing of laminates (Fig. 2.6a), the next step was to cut properly the specimens according to the standards used in this work. This section describes the operations to fabricate and the geometry of specimens used in the various tests.

2.3.1 Quasi-Static Tensile and Fatigue Specimens

The specimens for quasi-static and fatigue tests were made according to the standard ASTM D3039 [44] with a constant rectangular cross section (Fig. 2.6c). The measures are shown in Fig. 2.7.

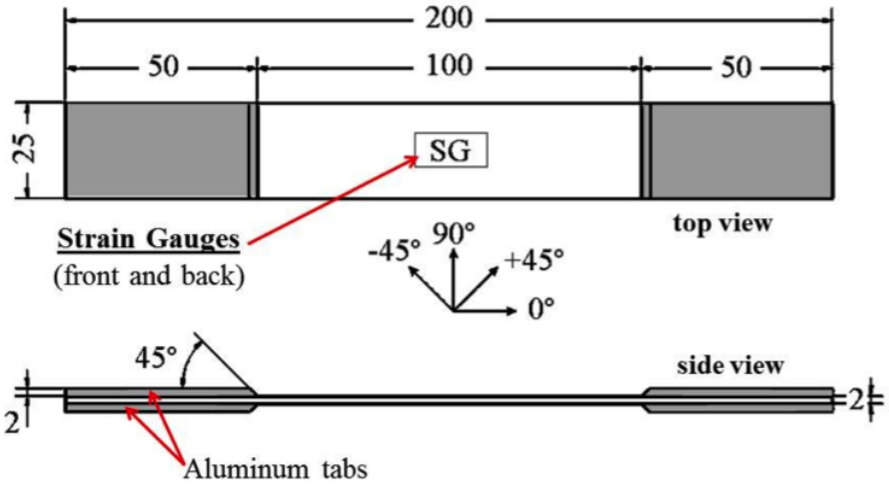

Figure 2.7: Quasi-stati and fatigue tensile specimen, measures are in mm; the strain gauges are applied only for quasi-static tests.

A diamond milling machine (Fig. 2.6b) was used to cut the laminate sheet into the specimens. The diamond blade was cooled with water to avoid heat damage to the matrix and fibers during cutting procedure. After cutting, the specimens were labelled according to their matrix composition (Table 2.7) and with a progressive number.

Tabs were prepared from an aluminum sheet of 2 mm thickness using a shearing machine, then the 45° chamfer was made. With a sandpaper sheet the roughness of the tabs surfaces were increased and then were glued with the Araldite^{TM} ST170, a bi-component epoxy glue. Finally, the specimens were rest for 24 h curing of the adhesive before starting the tests.

2.3.2 Short Beam Specimens

The specimens for short beam tests were made according to the standard ASTM D2344 [45] with a constant rectangular cross section. The measures are shown in Fig. 2.8a.

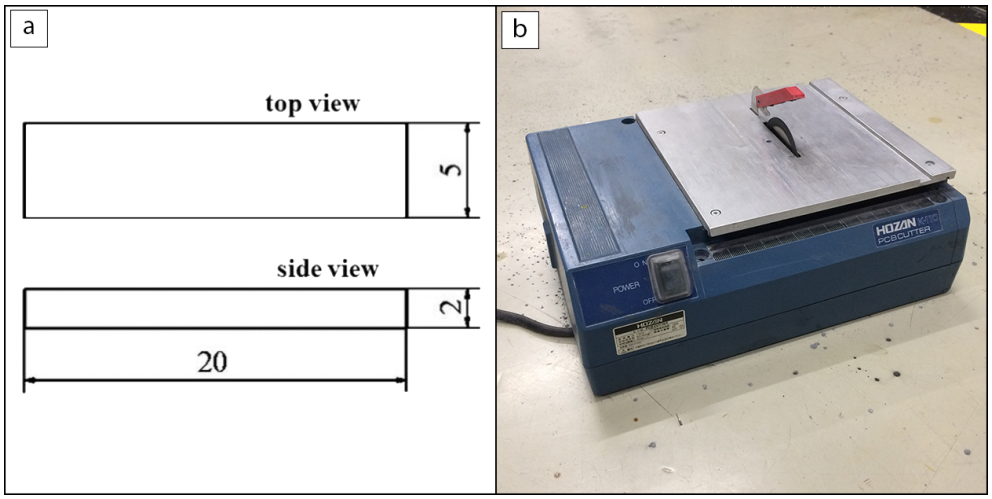

Figure 2.8: (a) Short beam specimen, measures are in mm; (b) PCB cutter with diamond blade.

A PCB cutter with a diamond blade (Fig. 2.8b) was used to cut the laminate sheet into specimens. Since the small size of specimens there was no need to cool down the blade during cutting, observations with an optical microscope (see section 3.7) were made in order to determine the presence of significant damage with respect to a cooled blade.

2.3.3 Impact Specimens

The specimens for impact tests were made according to the standard JIS K 7062 [46] with a constant rectangular cross section. The measures are shown in Fig. 2.9.

A diamond milling machine (Fig. 2.6b) was used to cut the laminate sheet into the specimens. The diamond blade was cooled with water to avoid heat damage to the matrix and fibers during cutting procedure. After cutting, the specimens were labelled according to their matrix composition (Table 2.7) and with a progressive number.

2.3.4 Specimens Dimension

The measuring of width and thickness was performed with a digital caliper with an accuracy of 0.01 mm in three different points through the total length of the specimens. In Table 2.9 are reported the actual geometry of specimens after measuring.

Test	Length [mm]	Width [mm]	Thickness [mm]
Quasi-static & fatigue	≈200	24.90 ± 0.20	1.95 ± 0.07
Short beam	≈ 20	4.99 ± 0.05	2.00 ± 0.07
Impact	≈ 65	13.48 ± 0.21	1.95 ± 0.11

Table 2.9: Measured dimension with standard deviation of specimens.

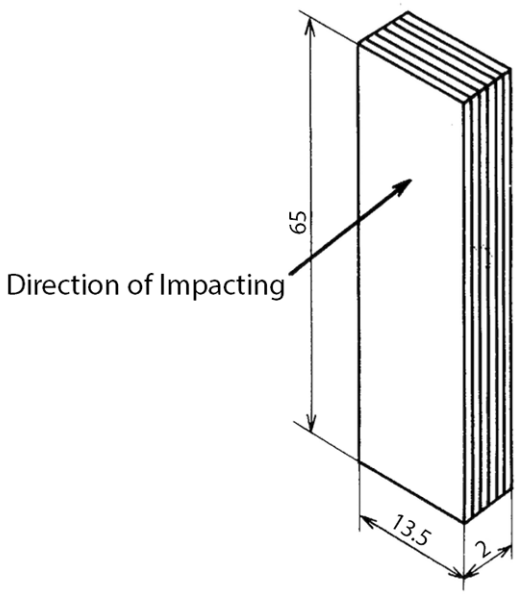

Figure 2.9: Impact specimen, measures are in mm.

Chapter 3

Experimental Devices and Setups

This chapter describes the equipment used for the various experimental activities.

3.1 Quasi-Static Tensile Tests

Quasi-static tensile tests were performed according to the standard ASTM D3039 [44] using a mechanical universal testing machine, the Shimadzu Autograph AG-IS [47]. The machine was equipped with a load cell having a capacity of 100 kN. Non-shift wedge type grips were mounted to grab the specimens (Fig. 3.1b).

The specimens dimension are described in section 2.3.1, they have a gage length of 100 mm. To get accurate measurements of strain two strain gauges were applied for each specimen (Fig. 3.1a). The gauges were applied on bot the surfaces of the specimen in the middle of the gage length and centered with respect to the width of the sample (Fig. 2.7). The properties of strain gauges Kyowa KFRP 5-120-C1-3L2M2R are reported in Table 3.1. Kyowa adhesive CC-33A was used to apply them on the surface of specimens.

Gage Length [mm]	**Gage Factor** at 25 °C, 50% RH	**Gage Resistance** [Ω]
5	1.98 ± 0.02	120.0 ± 0.8

Table 3.1: Main physical properties of strain gauges.

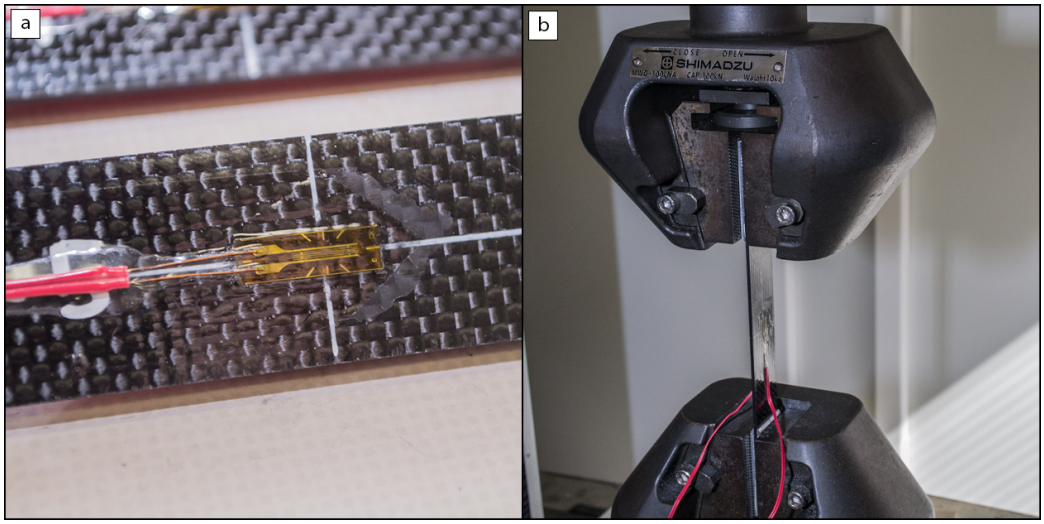

Figure 3.1: (a) Particular of the strain gage applied to a specimen and (b) specimen mounted on the testing machine.

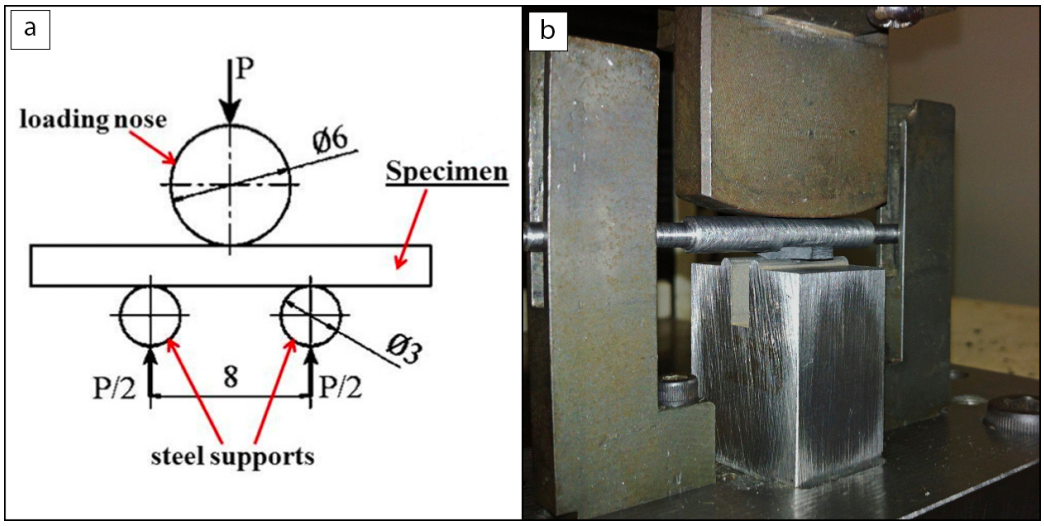

Figure 3.2: (a) Loading condition for short beam tests and (b) picture of specimen during a test.

The loading was performed in stroke control, with a cross head speed set to 1 mm/min. The data were acquired with two data logger PCD300B and PCD320A provided by Kyowa Electronic Instruments Co. Ltd. [48]; the first, PDC 300B, was connected directly to the strain gauges with 1/4 of bridge, while the second, PCD 320A, was connected to the machine to get data from load cell and the transducer for the stroke. The acquisition software was provided by Kyowa Electronic Instruments Co. Ltd. (DCS-100A [49]).

3.2 Short Beam Tests

Short Beam tests were performed according to the standard ASTM D2344 [45] using a mechanical universal testing machine, the Shimadzu Autograph AG-IS [47]. The machine was equipped with a load cell having a capacity of 100 kN. The loading scheme is shown in Fig. 3.2a. The lower metal support in Fig. 3.2b was designed and realized in the workshop specifically for this test.

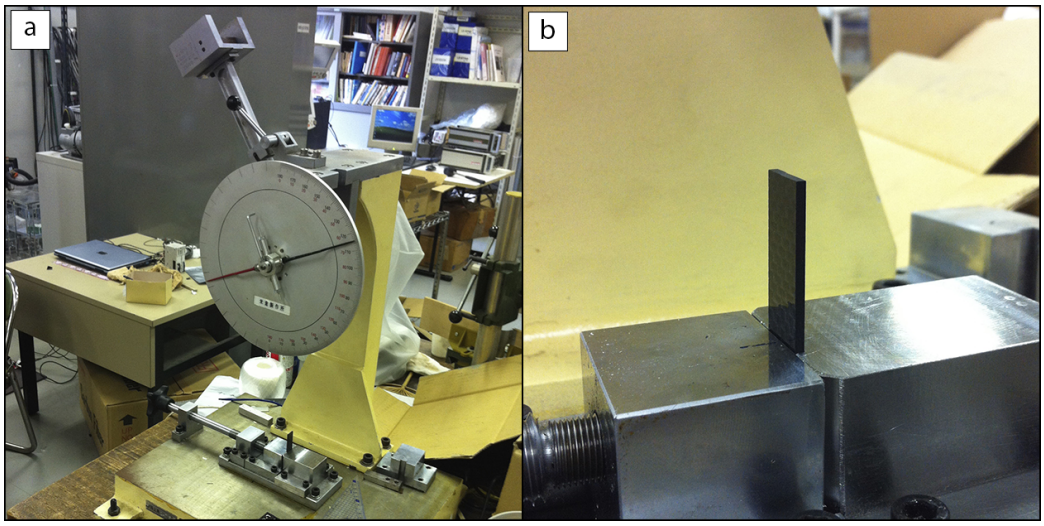

Figure 3.3: (a) Izod testing machine and (b) a specimen ready for test.

The loading was performed in stroke control, with a cross head speed set to 1 mm/min. The data were acquired with a data logger PCD320A provided by Kyowa Electronic Instruments Co. Ltd. [48]; connected to the machine to get data from load cell and the transducer for the stroke. The acquisition software was provided by Kyowa Electronic Instruments Co. Ltd. (DCS-100A [49]).

3.3 Impact Tests

Impact tests were performed according to the standard JIS K 7062 [46] using an Izod pendulum (Fig. 3.3a) at room temperature and direction of blow normal to the plane of reinforcement (Fig. 3.3b). The hammer of the impact test machine had a mass of 2.106 kg and an arm of 30.7 cm.

For these measurements the data are collected reading the angle value on the graduate scale of the device.

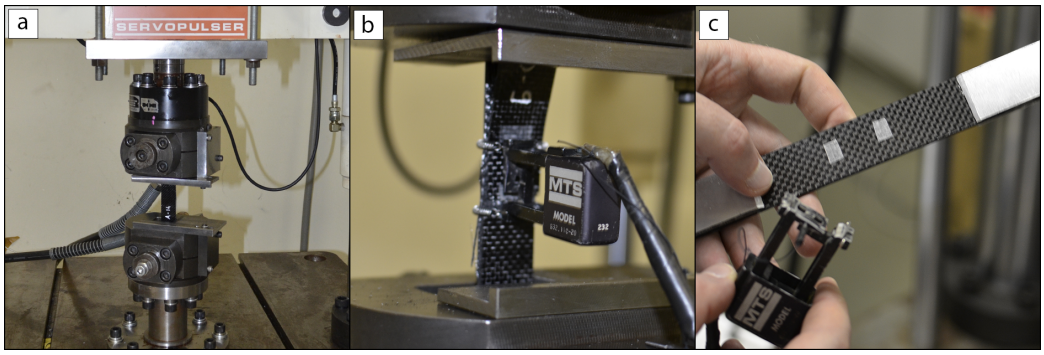

Figure 3.4: (a) Servopulser testing machine with mounted specimen, (b) extensometer attached to a specimen after failure and (c) application of extensometer to specimen with double-sided adhesive tape.

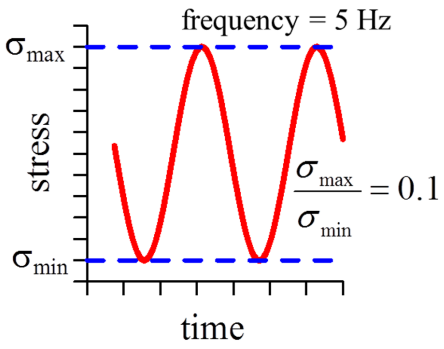

Figure 3.5: Loading condition for tensile-tensile fatigue tests.

3.4 Tensile Fatigue Tests

Tension-tension fatigue tests were performed according to the standard ASTM D3479 [50] using an hydraulic universal testing machine, the Shimadzu Servopulser EHF-UB50KN-20L [51] (Fig. 3.4a). The machine was equipped with a load cell having a capacity of 50 kN. Hydraulic jigs were mounted to grab the specimens.

The cyclic loading was performed under constant stress amplitude, sinusoidal wave-form tensile- tensile loading and assuming the ratio $R = 0.1$ (ratio of the minimum to the maximum stress in the cycle). The frequency

was set to 5 Hz (Fig. 3.5). Three different maximum stress levels were considered: 80%, 75% and 70% of the ultimate static tensile stress σ_u (see Table 4.1).

During cyclic loading the strain in the load direction was measured by an MTS extensometer (mod. 632.11C Fig. 3.4b) with gage length of 20 mm and for some specimens by Digital Image Correlation (DIC, see section 3.5); in order to avoid the slipping of extensometer's blades two small pieces of double-sided adhesive tape were attached to the specimens surface as shown in Fig. 3.4c. The data were acquired with two data logger PCD300B and PCD320A provided by Kyowa Electronic Instruments Co. Ltd. [48]; the first, PDC 300B, was connected directly to the extensometer, while the second, PCD 320A, was connected to the machine to get data from load cell and for stroke. The acquisition software was provided by Kyowa Electronic Instruments Co. Ltd. (DCS-100A [49]). The software was set to record an interval of 2 seconds every 2000 cycles for tests at 80%, 5000 cycles for tests at 75% and 10 000 cycles for tests at 70% of the ultimate static tensile stress σ_u.

3.5 Digital Image Correlation

Digital Image Correlation was used for measuring the full-field strain evolution during some fatigue tests. Fatigue tests were performed at 5 Hz; then, in order to record enough pictures for each cycle an high speed camera was used.

For the images recording a fx K3 high speed camera by nac Image Technology. Inc. [52] was adopted. The camera has a maximum recording speed of 10 000 fps. For this work the recording frame rate was set to 250 fps to

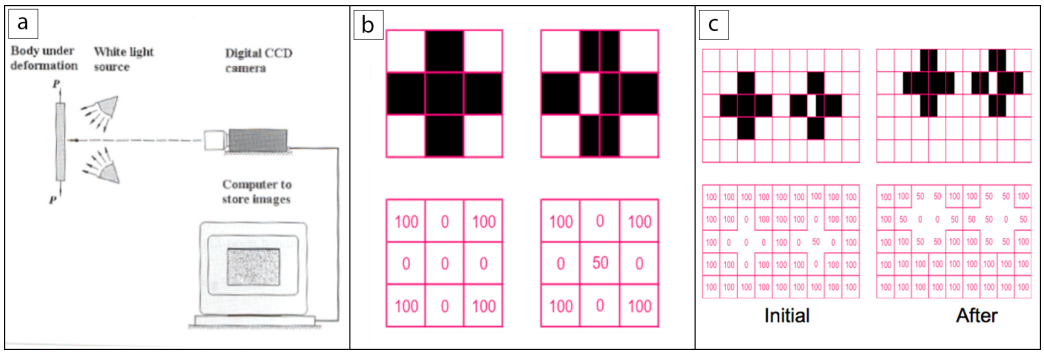

Figure 3.6: (a) Experimental setup for DIC measurements, (b) subset value assignement and (c) tracking of displacements according to subset movement.

have 50 pictures per cycle. The camera needs a huge amount of light, then a spotlight, directed on the specimen, was used to achieve the best lighting condition. A small fan was added to avoid heating effect due to the spotlight light beam direct on the specimen (Fig. 3.7a).

Digital Image Correlation (often referred to as DIC) is a contact-less method which measures deformation on an object's surface. The method tracks the changes in gray value pattern in small neighborhoods called subsets during deformation (Fig. 3.6). With this technique it is possible to obtain a full-field value of the investigated area, and then, to determine where and when the damage will nucleate and grow during the cyclic loading.

The VIC-2D commercial software was used in this work for the images elaboration in order to obtain the displacement and strain field map [53]. The specimens needed to be prepared with a speckled pattern (Fig. 3.7b). First the specimen was painted with an acrylic white paint for 40 mm centered in the gage length. Then the pattern was created spraying black acrylic paint. The result pattern had to be uniform and random; the dimension of the points onto the pattern has to be chosen according to the expected value of strain that will be measured.

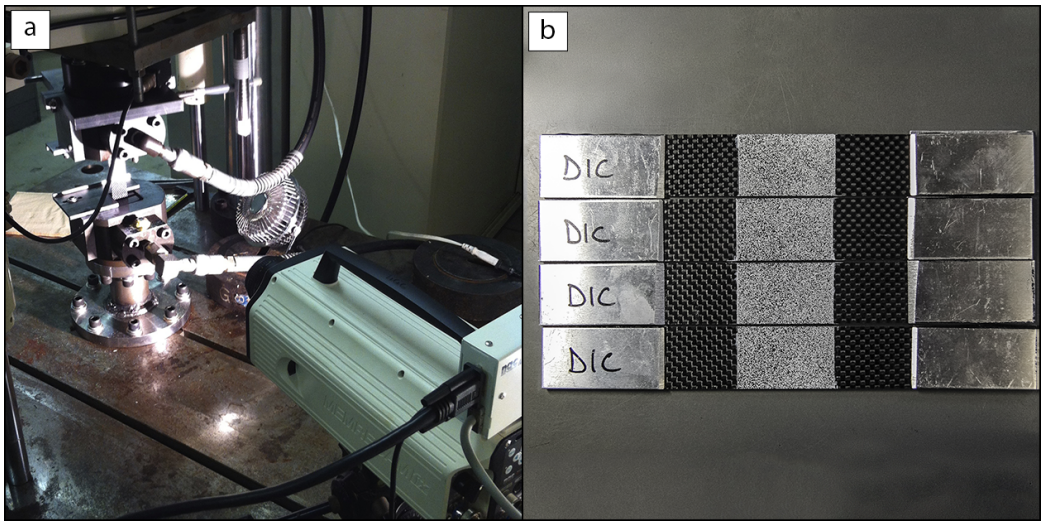

Figure 3.7: (a) Setup for high speed camera acquisition and (b) specimens with pattern for DIC.

This technique was used only for some tests at 80% of the ultimate static tensile stress σ_u. Pictures were recorded every 2000 cycles, recording for 1.5 seconds, which is the maximum capacity of the camera at that specific frame rate.

3.6 Thermal Camera

To further investigate the initiation and propagation of damage a thermal camera was adopted for some cyclic tests. With the temperature map of the specimens surface it is possible to determine the initiation of the damaged zone and the propagation during the cyclic tests (Fig. 3.8a).

A Flir SC7000 infrared camera was used to get the temperature map on specimens surface [54]. For the correct reading of the temperature the specimens needed to be prepared (Fig. 3.8b). A matte black paint was sprayed on the surface to avoid reflections and obtain a uniform emissivity; reflections can cause misreading in the infrared camera.

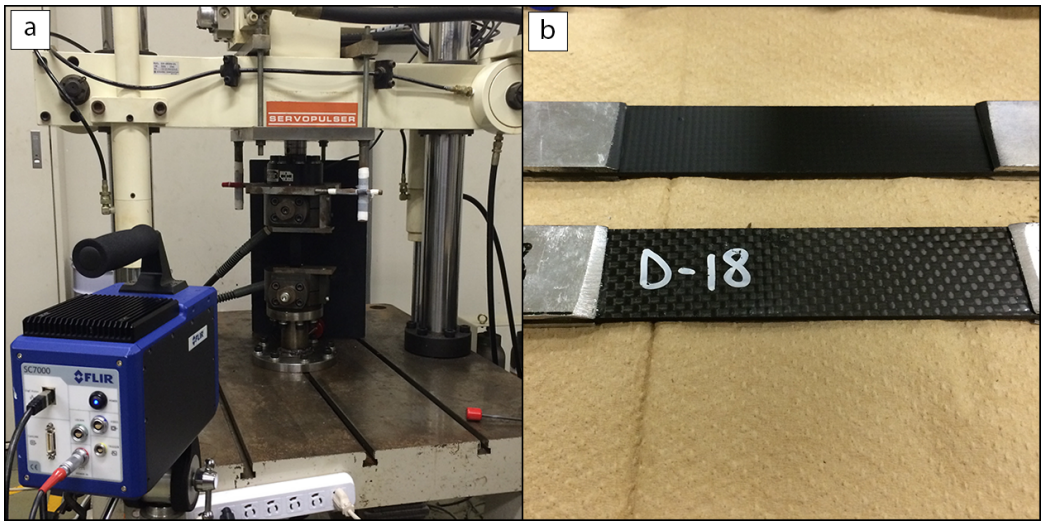

Figure 3.8: (a) Setup for thermal camera acquisition and (b) specimens before (lower) and after (upper) matte black painting.

This technique was used only for some tests at 80% and 75% of the ultimate static tensile stress σ_u. Pictures were recorded every 2000 cycles for 80% and every 5000 cycles for 75%. For each interval 2 seconds at a frame rate of 250 fps were recorded.

3.7 Optical Microscope

An optical microscope was used to observe the failure mechanism after short beam tests. The Keyence VHX-2000 microscope [55] is used equipped with the Keyence lens VH-Z100R [56].

Specimens for optical microscope were cleaned before the observations.

3.8 Scanning Electron Microscope

A Scanning Electron Microscope (SEM) was exploited to investigate the fracture surface of some specimens after quasi-static and fatigue tensile tests.

Resolution		**Magnification**		**Accelerating Voltage**
nm @ 30 kV	nm @ 1 kV	From	To	kV
1.2	3.0	×10	×1 000 000	0.5 to 30

Table 3.2: Main parameter for scanning electron microscope [57].

The JSM-7001F Schottky emission SEM provided by JEOL inc. was used in this study [57]. Some of the principal specifications of JSM-7001F SEM are reported in Table 3.2.

The measurements were performed with the acceleration voltage in the range of $10 \div 15$ kV. Specimens for SEM observation had maximum dimensions of $10 \times 10 \times 5$ mm; they were mounted on specific support. For conventional SEM imaging the samples must be electrically conductive, at least at the surface, and electrically grounded to prevent the accumulation of electrostatic charge at the surface. For this reason all the specimens were coated with a gold layer 150 nm thick using an ion sputtering device.

Chapter 4

Results and Discussion

In this chapter the results of the experimental investigation are shown and discussed. Moreover, the microscopical observations are presented to highlight the failure mechanism and understand how the fillers can contribute in changing the mechanical behavior of the considered composite materials.

4.1 Quasi-Static Tensile Tests

According to the standard ASTM D3039 [44] five specimens for each combination of fillers content were tested. The complete set of twelve different combinations of MFC and XNBR contents in epoxy resin were adopted, for a total of 60 quasi-static tensile tests.

In order to determine the correct loading and alignment of the specimens two strain gauges were used, one on each side of the sample. In Fig. 4.1 is shown the comparison between front and back strains for some specimens of different fillers content. The good agreement between the two strains confirms the correct preparation and execution of quasi-static tensile tests.

Stress-strain curves for some specimens of different fillers contents are

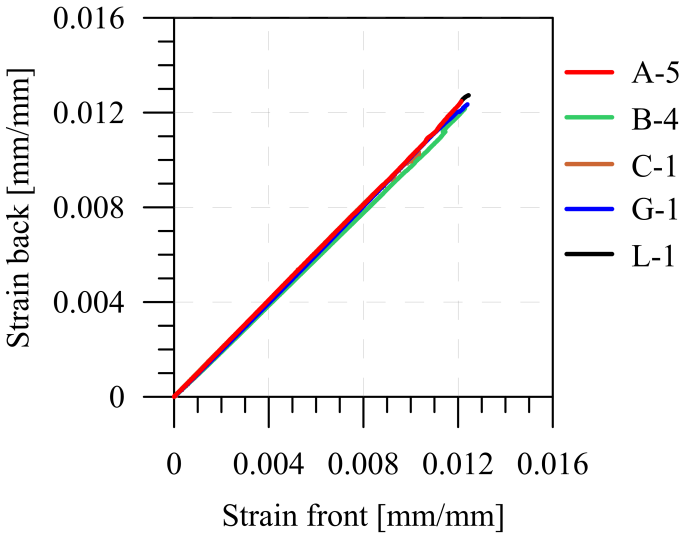

Figure 4.1: Comparison of the two strain gauges measurements for some specimens.

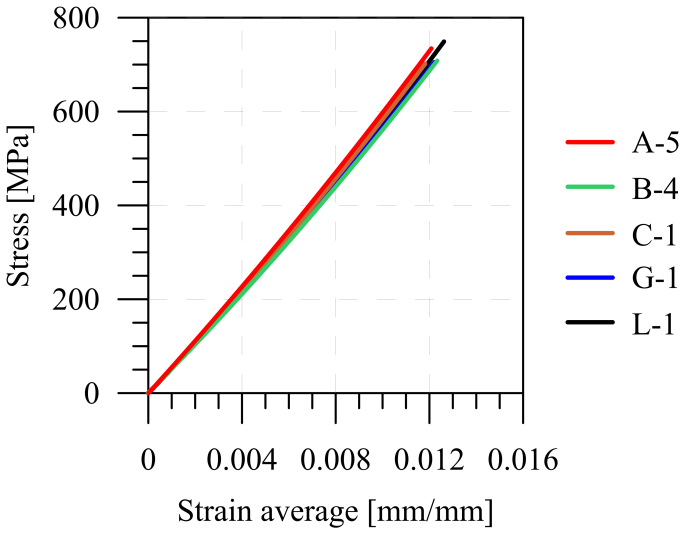

Figure 4.2: Comparison of stress-strain curves for some specimens.

shown in Fig. 4.2. They are almost linear. However, when the tangent modulus is considered (Fig. 4.3), the non linearity is evident. This is probably due to two factors: the inherent stiffening of carbon fibers under tensile loading and the non-linearity due to the weave structure of carbon fabrics. The inherent stiffening was presented in [58], and explained by a change of crystalline orientation of carbon fibers in reference [59]. This effect was confirmed in many experimental studies such as [60] and [61].

The effect of fillers on the tensile mechanical properties is highlighted comparing the Young's modulus (the initial secant modulus is considered according to standard ASTM D3039 [44]) and the tensile strength. Figures 4.4 and 4.5 present the average value of those mechanical features for the considered fillers contents.

Compared to the composite with pure epoxy resin (material A, see Table 2.7) the combination of MFC and XNBR does not provide relevant variations of the material stiffness. The recorded values remains in the same experimental scatter band (Figs. 4.5 and 4.4b) Similar results are obtained in [22] with MFC filler.

More interesting effects are observed for the tensile strength. The only filler XNBR does not have a positive effect. It produces a slight reduction of the tensile properties with increasing the content as shown in Fig. 4.5a where the MFC content is kept constant at 0.0 wt%. Adding only MFC, without XNBR filler as shown in Fig. 4.4a for 0 wt% XNBR, has a considerable improvement (5%) for content of 0.3 wt% MFC which corresponds to material C (see Table 2.7).

When the two fillers are both added in the epoxy resin for some contents the tensile strength enhances compared to the material with pure matrix. Setting MFC at 0.1 wt%, the coupling with 1 wt% of XNBR gives a reduction

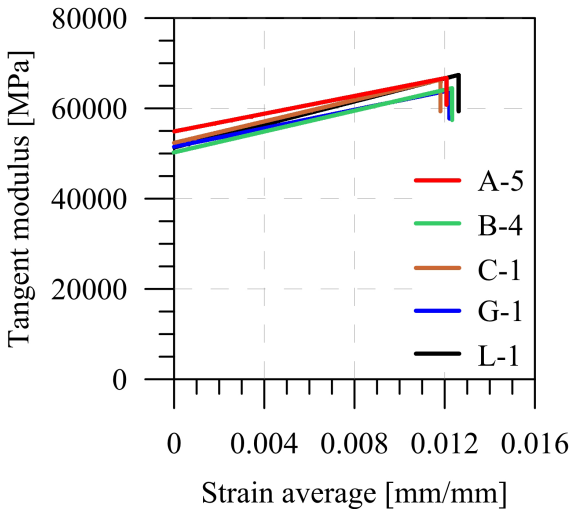

Figure 4.3: Fitting of the tangent modulus vs. strain for some specimens.

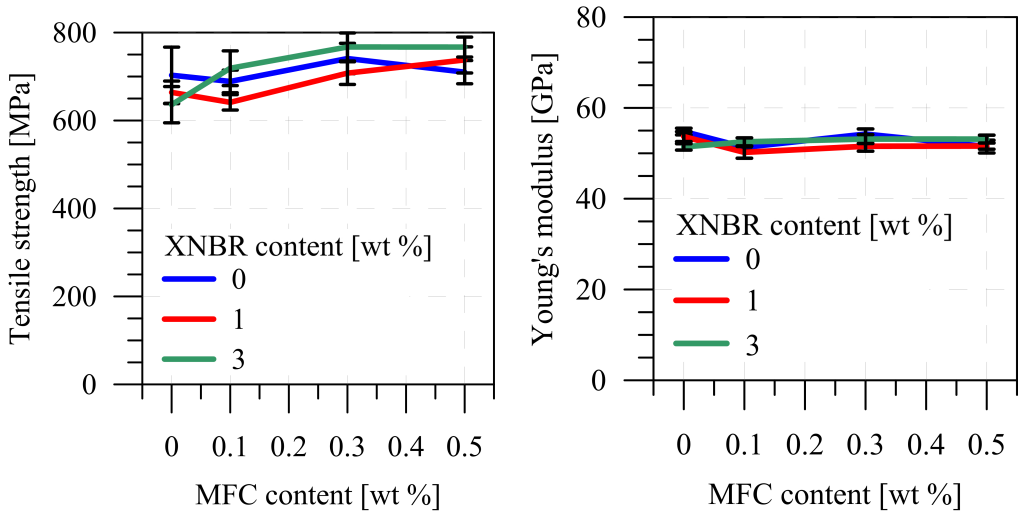

(a) (b)

Figure 4.4: (a) Young's modulus and (b) tensile strength for constant XNBR contents. Bars indicate standard deviation.

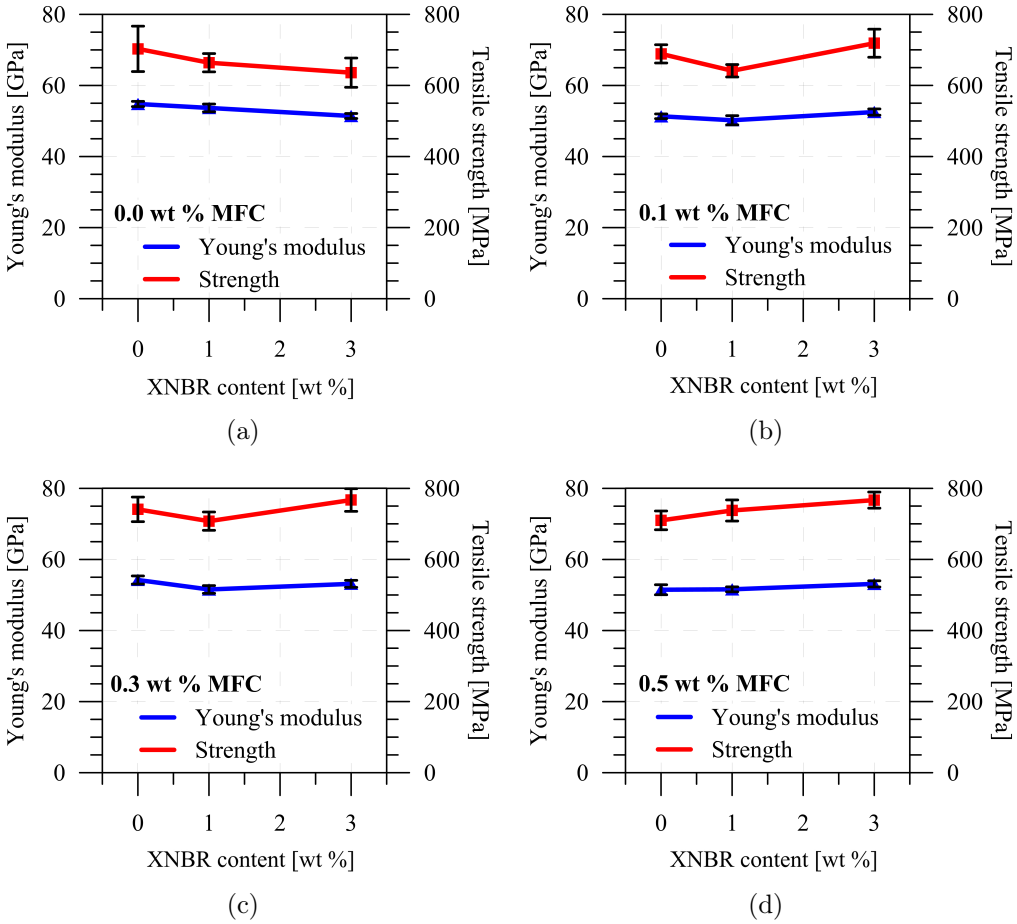

Figure 4.5: Young's modulus and tensile strength for (a) 0.0 wt% MFC, (b) 0.1 wt% MFC, (c) 0.3 wt% MFC and (d) 0.5 wt% MFC. Bars indicate standard deviation.

	MFC			
XNBR	0.0 wt%	0.1 wt%	0.3 wt%	0.5 wt%
0 wt%	703.0 ± 63.9	688.9 ± 25.7	741.0 ± 34.6	710.0 ± 26.4
1 wt%	664.0 ± 25.7	641.3 ± 17.5	707.8 ± 25.8	737.8 ± 29.7
3 wt%	636.0 ± 41.2	718.9 ± 39.5	767.2 ± 31.9	767.0 ± 22.7

Table 4.1: Average tensile strength σ_u [MPa] with standard deviation for the twelve different combinations of fillers.

	MFC			
XNBR	0.0 wt%	0.1 wt%	0.3 wt%	0.5 wt%
0 wt%	54.8 ± 0.7	51.3 ± 0.7	54.2 ± 1.1	51.5 ± 1.4
1 wt%	53.7 ± 1.1	50.2 ± 1.3	51.6 ± 1.1	51.6 ± 0.7
3 wt%	51.4 ± 0.7	52.5 ± 0.9	53.1 ± 1.0	53.1 ± 0.9

Table 4.2: Average Young's modulus [GPa] with standard deviation for the twelve different combinations of fillers.

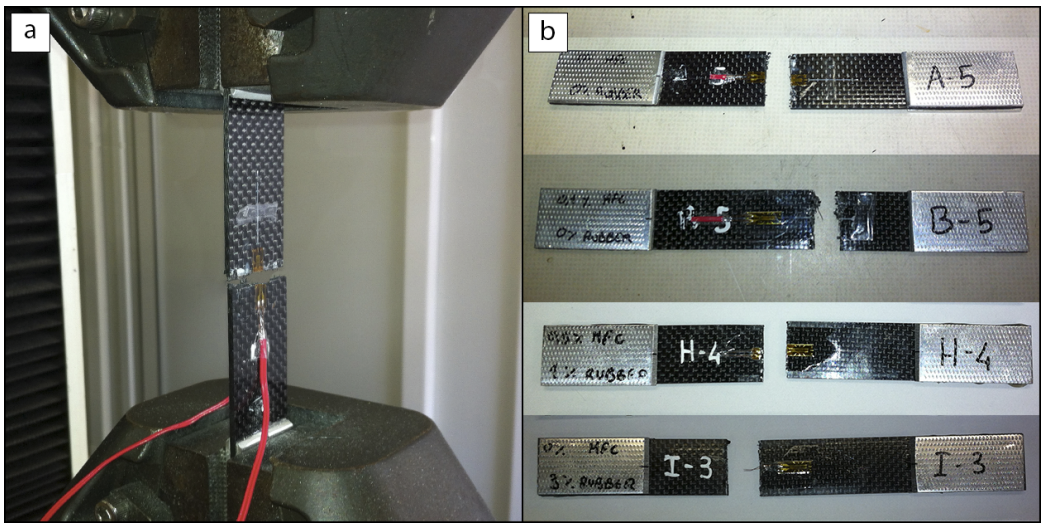

Figure 4.6: (a) Specimen failure right after the test and (b) some specimens failure mode: from the top materials A, B, H and I according to Table 2.7.

of strength, while for 3 wt% of XNBR an increase of 3 % is recorded (Fig. 4.5b). MFC content of 0.3 wt% does not increase the strength using 1 wt% of XNBR, while with 3 wt% of XNBR (material K according to Table 2.7) the strength increases about 10 % (Fig. 4.5c). If MFC is 0.5 wt%, a continuous enhancement of the tensile strength is recorded: 5 % and 10 % with 1 wt% and 3 wt% of XNBR, respectively (Fig. 4.5d and Fig. 4.4a).

In Tables 4.1 and 4.2 are reported the average values of the tensile strength and the Young's modulus, respectively.

4.1.1 SEM Observations

The improvement of the tensile strength, with content of 0.3 wt% MFC and 3 wt% XNBR, finds some motivation observing the failure mechanism. The global failure mode of the tensile specimens is, according to standard ASTM D3039 [44], of the type LGM (lateral, gage, middle). It does not reveal the influence of the fillers (see e.g. the pictures in Fig. 4.6). Scanning electron microscope images of specimens after tensile failure, for some combinations of MFC and XNBR contents, demonstrate the influence of fillers (Figures 4.7, 4.8 and 4.9).

All contents show clearly fiber pull out at the fracture surface as well as carbon fiber breakage. Three main differences of the fracture surfaces are evident: the matrix deformation, the residual matrix on the fibers surface and the de-bonding at the interface matrix-fiber.

The matrix has a brittle failure in the unfilled material (Fig. 4.7a), while introducing MFC and XNBR the matrix shows a more "plastic" deformation. In Figure 4.7b the absence of MFC with 1 wt% of XNBR generates a slight increase of the matrix deformation. However this is not enough to affect the tensile strength. Filling the epoxy resin with 3 wt% of XNBR and MFC

in the range $0.1 \div 0.3$ wt%, the deformation observed in the matrix is very extensive. Figures 4.7c and 4.7d show the matrix fracture surface with several indentation, this is a symptom of a ductile behavior of the epoxy resin.

After failure,the fibers of the composite with pure resin show very clean surfaces (see Fig. 4.8a), no residual parts of resin are evident on the fiber surface. Increasing the content of MFC and XNBR, the quantity of matrix attached to fibers after failure increases as shown in Figures 4.8b and 4.8c. A complete adhesion fiber matrix is evident for material K (0.3 wt% of MFC and 3 wt% of XNBR) as shown in Figure 4.8d.

The improved strength of the interface fiber-matrix due to fillers is evident looking at the failure surface of longitudinal fibers. For the unfilled epoxy resin the de-bonding is evident as shown in Fig. 4.9a. Adding only XNBR improves the interface strength, but some de-bonding still remain (Fig. 4.9b). The best performance is achieved with materials J and K (MFC $0.1 \div 0.3$ wt% and XNBR 3 wt%) where no de-bonding at the interface is observed (Fig. 4.9c and 4.9d).

As consequence the fillers seem to have an important influence on the interface adhesion, as observed in [62]. This is in agreement with the increase of tensile strength measured for material J and K (see Fig. 4.4a). The mixture with 3 wt% XNBR and 0.3 wt% MFC shows the larger matrix deformability, the better fiber-matrix adhesion and, therefore, the higher tensile strength.

4.2 Short Beam Tests

According to the standard ASTM D2344 [45] ten specimens for each combination of fillers content were tested. The complete set of twelve different combinations of MFC and XNBR contents in epoxy resin were adopted, for

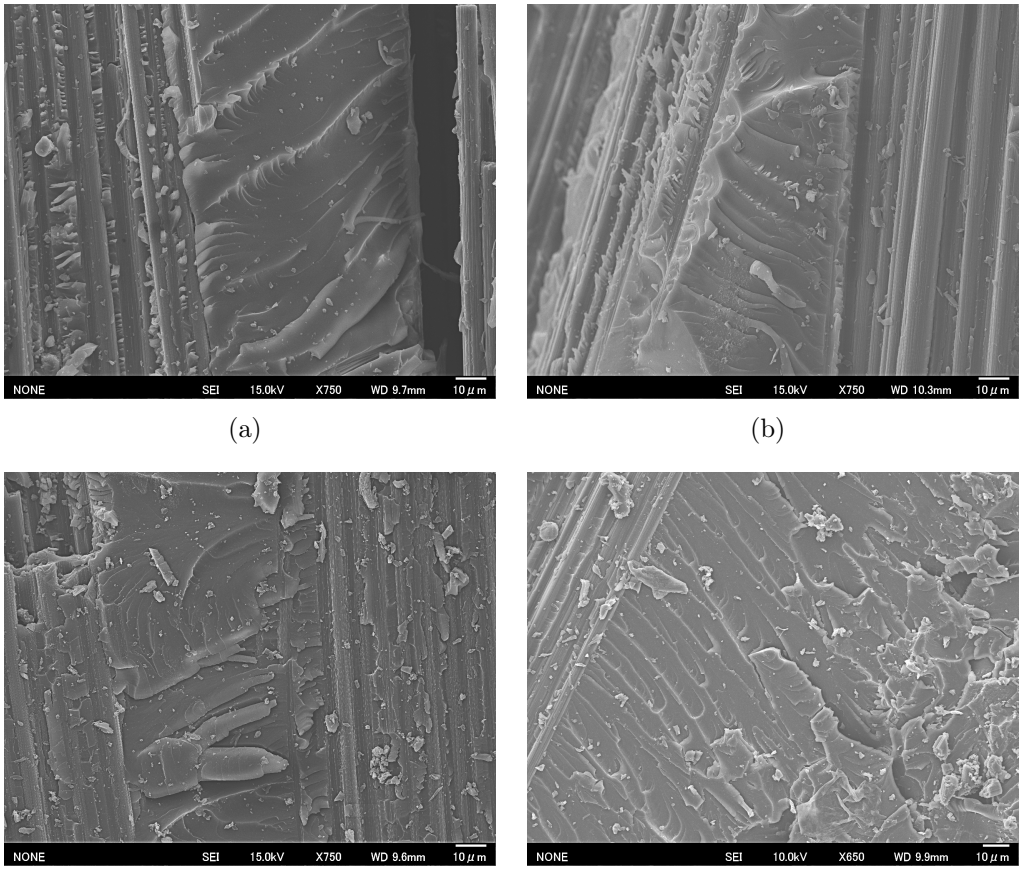

(a) (b)

(c) (d)

Figure 4.7: SEM pictures of the tensile failure surface for filler content (a) A; (b) E; (c) J and (d) K according to Table 2.7.

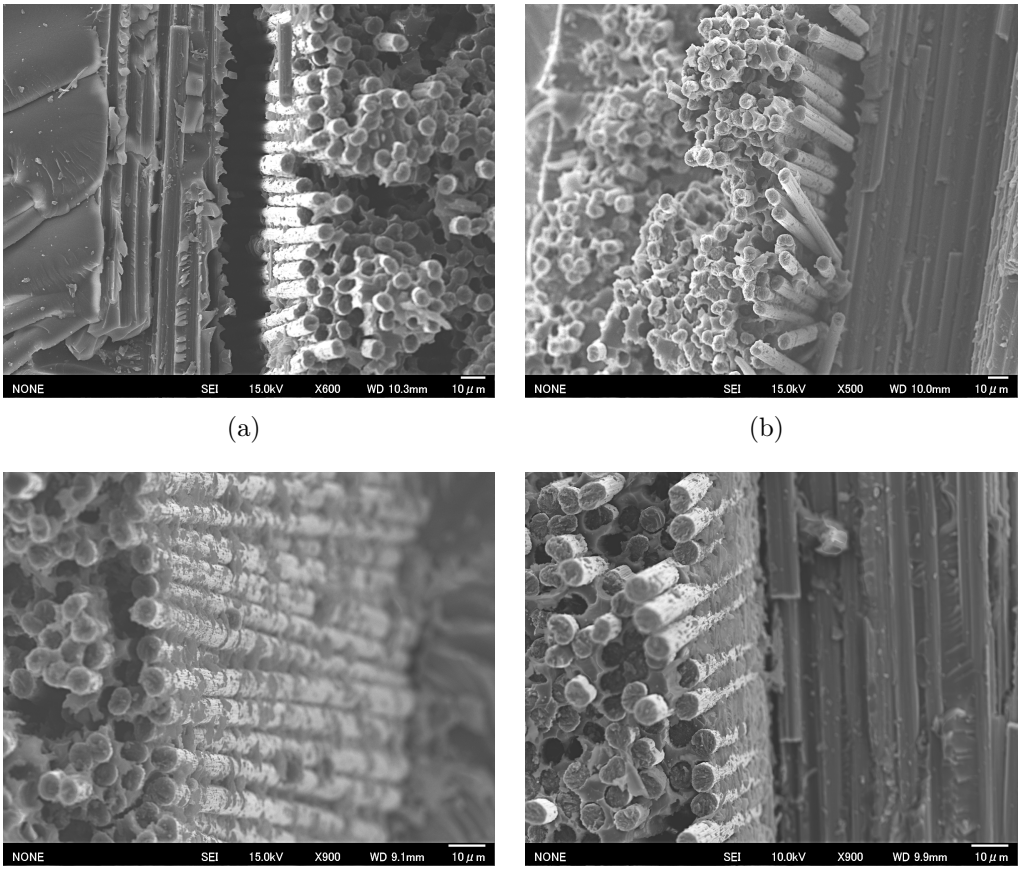

(a) (b)

(c) (d)

Figure 4.8: SEM pictures of the tensile failure surface for filler content (a) A; (b) E; (c) J and (d) K according to Table 2.7. Pictures are focused on the pulled out fibers of the failure surface.

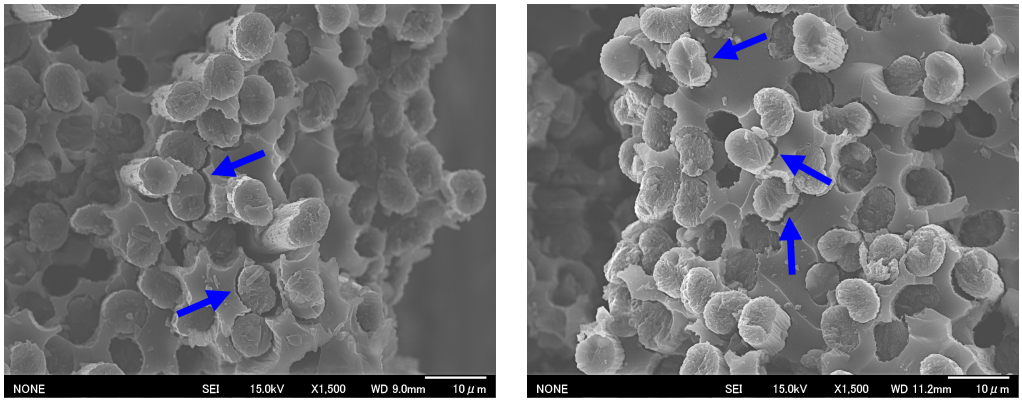

(a) (b)

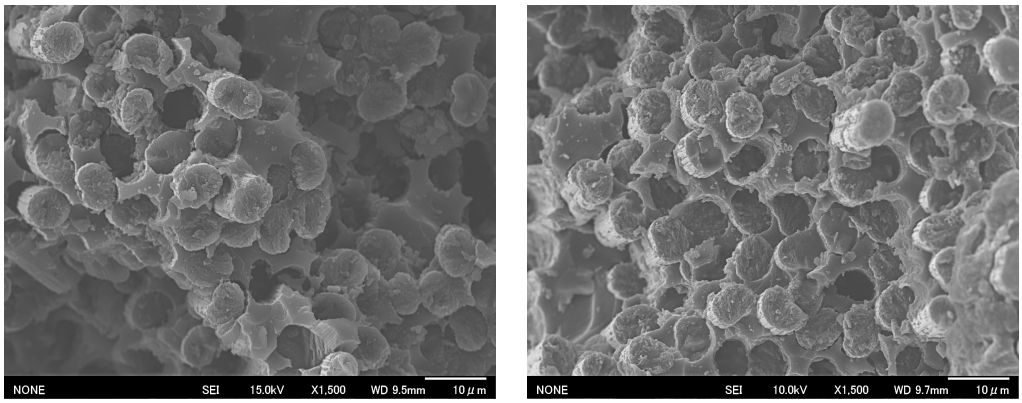

(c) (d)

Figure 4.9: SEM pictures of the tensile failure surface for filler content (a) A; (b) E; (c) J and (d) K according to Table 2.7. The arrows highlight the de-bonding along the matrix-fiber interface.

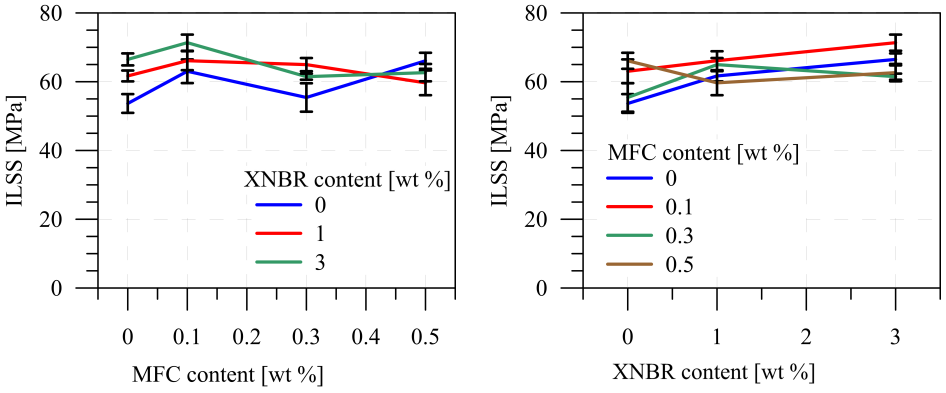

Figure 4.10: Inter-laminar shear strength tests results. Bars indicate standard deviation.

a total of 120 short beam tests.

The short beam tests are performed to determine the inter-laminar shear strength (ILSS), which is calculated as:

$$F^{sbs} = 0.75 \cdot \frac{P_m}{b \cdot h} \tag{4.1}$$

where, F^{sbs} is the ILSS [MPa], P_m is the maximum load [N], b the measured specimen width [mm] and h the measured specimen thickness [mm] [45].

Short beam geometrical configuration maximizes the shear stress between the different layer of the composite, the ILSS value is a first estimation of the inter-laminar fracture toughness.

Figure 4.10 shows the average value of the inter-laminar shear strength for the considered MFC and XNBR filler contents, compared to the value of the material with pure epoxy resin (material A in Table 2.7). XNBR in the resin has a positive effect. The ILSS increases with an increase of XNBR nanoparticle. A similar trend is observed using only MFC, except for 0.3 wt%

content. The main effects, in term of ILSS, arise combining the two fillers. A negative contribution is observed filling the epoxy resin with 0.5 wt% MFC. In fact, the ILSS decreases adding XNBR nanoparticles.

The opposite behavior is observed setting the MFC content to 0.1 wt%. The ILSS is continuously enhanced increasing the quantity of XNBR. In particular, with 0.1 wt% MFC and 3 wt% XNBR the best performance was recorded (see Fig. 4.10). The increment of ILSS is higher than 32% with respect to the unfilled epoxy resin. To have an improvement of inter-laminar shear strength, for analyzed range of fillers contents, the mixture must have XNBR $\leq$3 wt% and MFC $\leq$0.3 wt%.

In Table 4.3 the average values of inter-laminar shear strength are reported.

	MFC			
XNBR	0.0 wt%	0.1 wt%	0.3 wt%	0.5 wt%
0 wt%	53.7 ± 2.7	63.0 ± 3.4	55.4 ± 4.1	66.1 ± 2.3
1 wt%	61.7 ± 1.6	66.1 ± 2.8	65.0 ± 1.9	59.7 ± 3.6
3 wt%	66.5 ± 1.7	71.4 ± 2.3	61.5 ± 0.9	62.2 ± 2.5

Table 4.3: Average ILSS [MPa] with standard deviation for the twelve different combinations of fillers.

4.2.1 Optical Microscope Observations

The macro failure mode of the specimens was investigated with an optical microscope. The failure mechanism is not affected by the filler content and involves cracks at the layer interfaces (see Fig. 4.11). According to the standard ASTM D2344 [45] the failure mode is classified as inter-laminar shear failure.

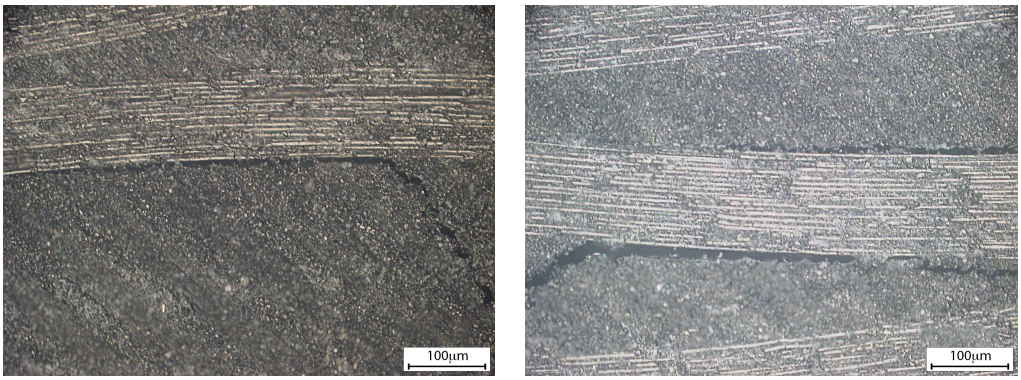

(a) (b)

(c) (d)

Figure 4.11: Optical microscope pictures of inter-laminar shear failure modes for filler content (a) A; (b) E; (c) J and (d) K according to Table 2.7.

4.3 Impact Tests

According to the standard JIS K 7062 [46] twelve specimens for each combination of fillers content were tested. The complete set of twelve different combinations of MFC and XNBR contents in epoxy resin were adopted, for a total of 144 Izod impact tests.

The absorbed energy, i.e. the energy needed to break the specimen, provides interesting trend of the impact strength in the considered range of the filler weight contents. It is calculated according to the standard JIS K 7062 [46] as:

$$E_{abs} = P \cdot D \cdot g \cdot \left[(\cos\beta - \cos\alpha) - (\cos\alpha' - \cos\alpha)\left(\frac{\alpha+\beta}{\alpha+\alpha'}\right)\right] \tag{4.2}$$

where, E_{abs} is the absorbed energy [J], P is the mass of the hammer [kg], D is the arm of the hammer [m], g is the gravitational acceleration [m/s^2], α is the angle by the hammer raised [°], α' is the angle made by swinging up when blank swing was done from the angle α of hammer raised [°] and β is the angle made by swinging up after the fracture was carried out [°] [46].

To better compare the values of the different specimens the Izod impact value, i.e. the specific absorbed energy which is calculated as:

$$a_I = \frac{E_{abs}}{b \cdot h} \tag{4.3}$$

where, a_I is the Izod impact value [J/mm^2], b is the measured specimen width [mm] and h is the measured specimen thickness [mm] [46].

The average Izod impact values are collected in Figure 4.12, where each curve represents a constant content of XNBR (Fig. 4.12a) and of MFC (Fig. 4.12b). A slight reduction of the strength with the unmodified material was

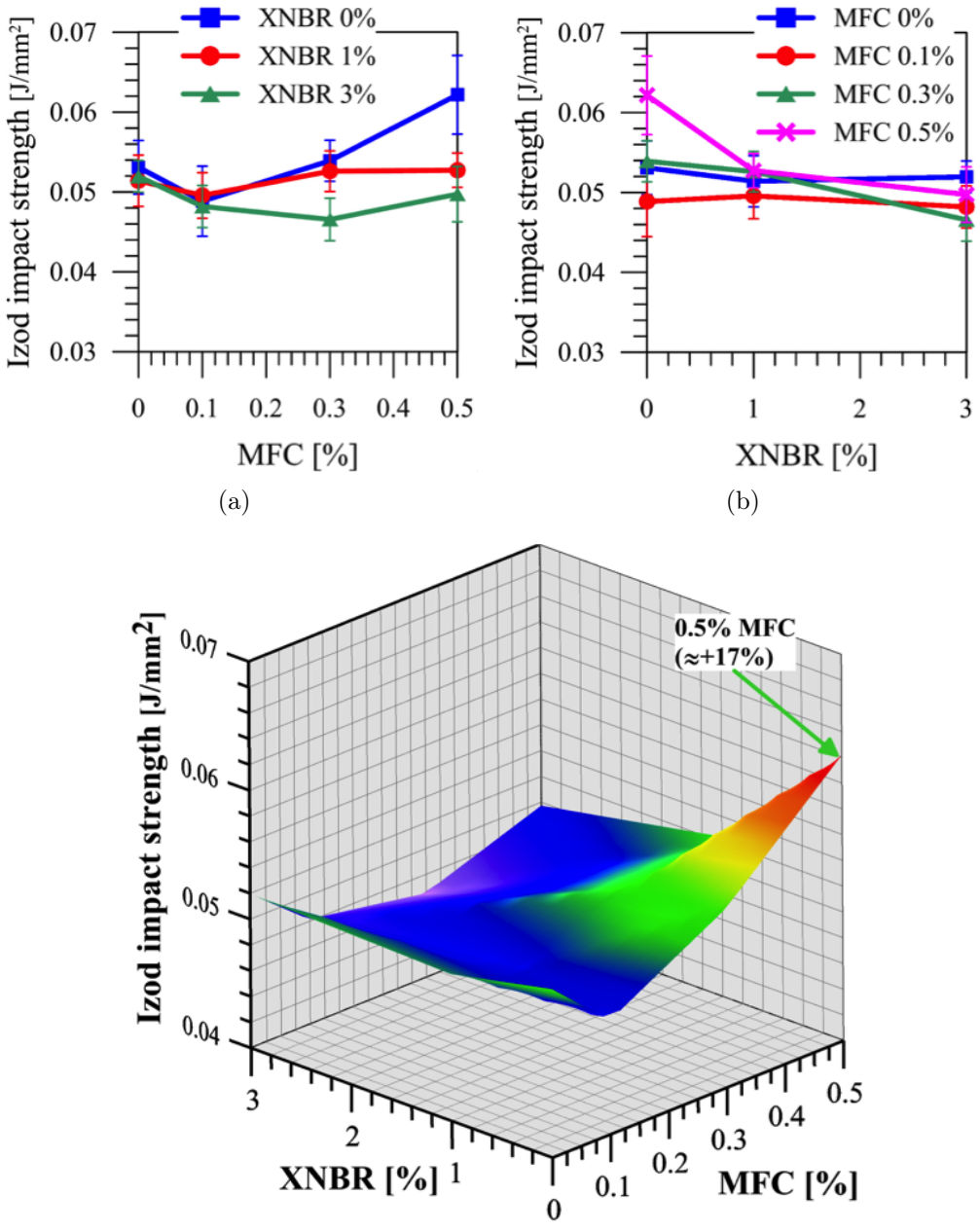

Figure 4.12: Average Izod impact value (a) vs. MFC content, (b) vs. XNBR content and (c) average surface fitting over the considered range of fillers content.

recorded for content of MFC in the range $0.1 \div 0.3$ wt% mixed with 3 wt% XNBR. The other combinations do not show considerable improvements or degradation of the impact strength, values are in the same experimental scatter band. The only important increase of the Izod impact value was obtained for the composite containing 0.5 wt% of MFC (material D according to Table 2.7), an enhancement of more than 17% compared to the unmodified composite. This clear trend is visible constructing the average surface in Figure 4.12c, which provides the Izod impact value for any combination of MFC and XNBR in the considered range.

For the sake of completeness in Table 4.3 are reported the average of Izod impact values.

	MFC			
XNBR	0.0 wt%	0.1 wt%	0.3 wt%	0.5 wt%
0 wt%	0.0531 ± 0.0034	0.0489 ± 0.0044	0.0539 ± 0.0026	0.0622 ± 0.0049
1 wt%	0.0514 ± 0.0032	0.0496 ± 0.0029	0.0526 ± 0.0025	0.0527 ± 0.0021
3 wt%	0.0520 ± 0.0020	0.0482 ± 0.0026	0.0466 ± 0.0027	0.0497 ± 0.0035

Table 4.4: Average Izod impact value (J/mm^2) with standard deviation for the twelve different combinations of fillers.

4.4 Tensile Fatigue Tests

According to the results of the previous measurements, some of the twelve compositions of fillers were chosen to perform the tensile-tensile fatigue tests.

In order to select the best performing material for quasi-static tensile and short beam tests, a rank is established as:

$$Rank = \left[\frac{(12 - P_{tens}) + (12 - P_{ilss})}{22} \right] \cdot 100 \tag{4.4}$$

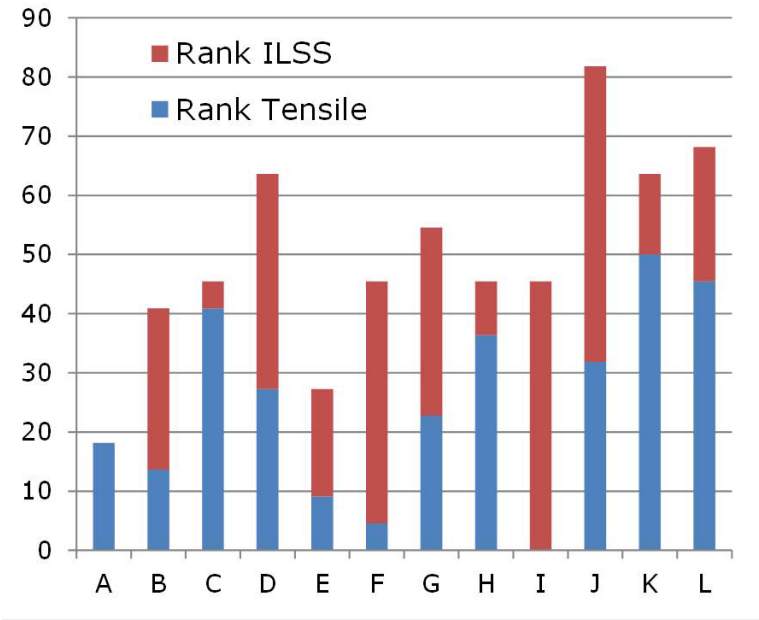

Figure 4.13: Histogram representing the rank evaluated with Equation 4.4 for the twelve considered composites.

where, *Rank* is a value between 0 and 100 (where 100 is the best performance), P_{tens} is the position of the material in the rank of the quasi-static tensile strength and P_{ilss} is the position of the material in the rank of the short beam tests. With this ranking a material had the best performance in one loading if gets a score of 50, while the worst performance is identify with score 0.

Material A, without any filler, was chosen as reference. Material D, J, K and L (see Table 2.7) were selected exhibiting the best static properties according to the rank (Fig. 4.13).

Three load levels were investigated: 80%, 75% and 70% of the quasi-static tensile ultimate stress σ_u (see Table 4.1). For each load at least three specimens were tested. For some load levels, additional tests were made using DIC or thermal camera. Cyclic tensile-tensile tests were performed up to the failure or up to 2 million cycles if complete failure did not occur.

Complete failure means separation in two parts of the specimen during cyclic loading. To avoid the influence of tab zones and grip pressure, a cyclic test was considered "valid" if the sample broke at a distance greater than 2 cm from the tabs.

The tensile-tensile fatigue tests performed in the considered stress range enable for depicting a Wöhler-type diagram for each of the five selected composites. Diagrams in Figure 4.14 represent, for each material, the number of cycles to failure (fatigue life, N) for all the valid tests of the three maximum stresses σ_{max}.

Comparison of all fatigue life curves for the five composites is in Figure 4.15. In this diagram for each material the valid cyclic tests for each load level are considered, as in Figure 4.14, and the respective average static tensile strength (see Table 4.1) corresponding to the extrapolated lowest number of cycles, $N = 1$. Fitting was adopted for the experimental data to have a reliable prediction of the fatigue life corresponding to the other stress levels in the considered stress range, which were not directly determined by testing. The semi-logarithmic function adopted here is:

$$\sigma_{max} = k \cdot \log N + a \tag{4.5}$$

where k and a are parameters to be defined by the least square method (see Table 4.5), and N is the fatigue life for the considered material. The diagram in Figure 4.15 shows the fitting of the experimental results (run-outs are not included) in terms of linear segments. The quality of the fittings is related to the coefficient of correlation R^2 [63]. Values of R^2 close to 1 confirm the reliability of the fitting. The curves in Figure 4.15 have the coefficient of correlation in the range $0.94 \div 0.98$. The slope k of the linear fitting curves, listed in Table 4.5, shows similar value for the composite A, D and J while

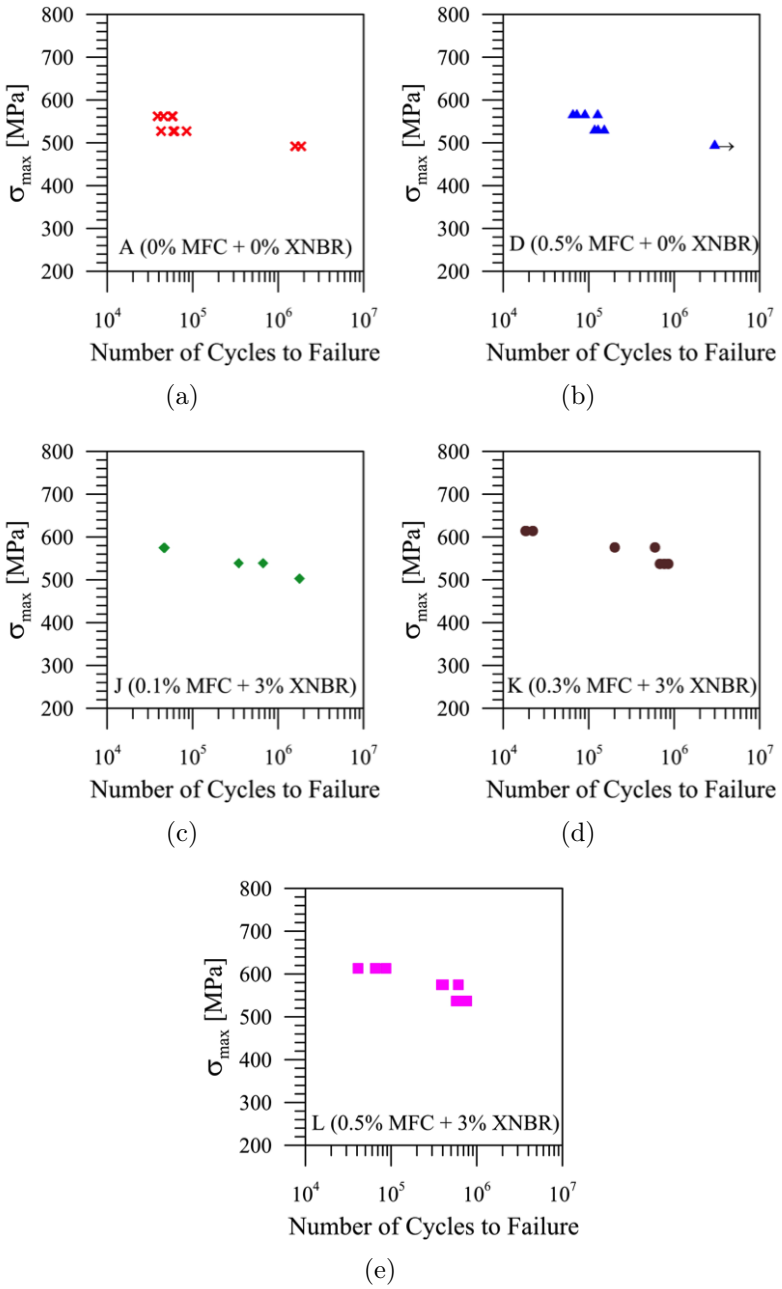

Figure 4.14: Maximum stress in the cycle vs. number of cycles to failure for material (a) A, (b) D, (c) J, (d) K and (e) L according to Table 2.7. → means no failure after 2 000 000 cycles.

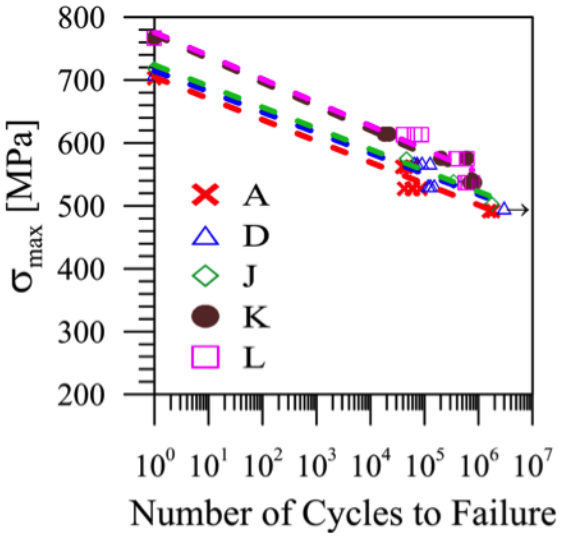

Figure 4.15: Maximum stress in the cycle vs. number of cycle to failure and semi-logarithm fitting for each composite. → means no failure after 2 000 000 cycles.

Material	k	a
A	14.64	704.6
D	14.23	714.8
J	14.54	723.6
K	16.43	771.6
L	16.12	775.6

Table 4.5: Parameters of the linear fitting of the fatigue life curves.

a 10% higher is for materials K and L. This predicts a fast reduction of the fatigue life in the range of high number of cycles for composites containing the higher content of both MFC and XNBR than that of the composites without XNBR. This is clear comparing in detail the average number of cycles to failure for three applied load levels in Figure 4.16.

The covariance of fatigue life in Figure 4.16 is in the range 0.2% ÷ 28%. In the low and medium cycles regimes (σ_{max} 80% and 75% of σ_u, Figures 4.16a and 4.16b) the fatigue life of composites with mix of the two fillers K and L

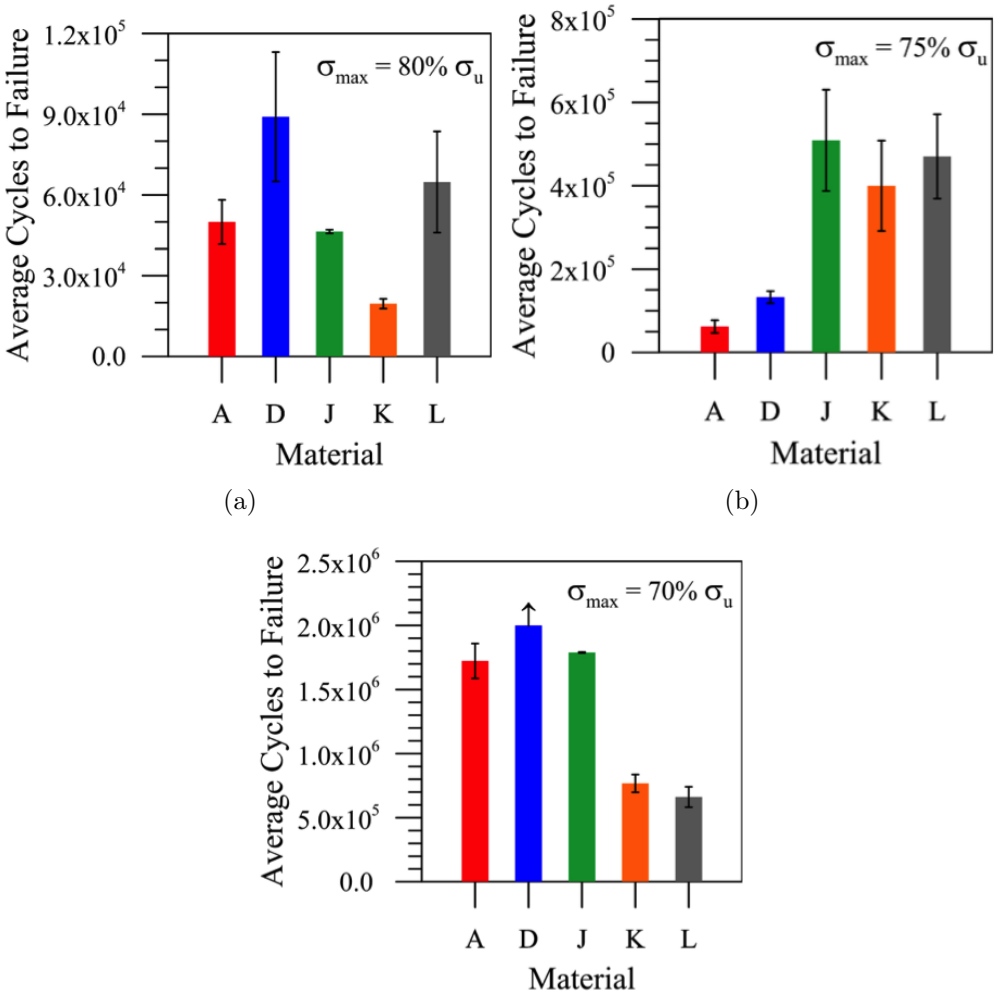

Figure 4.16: Comparison on the average fatigue life for the three maximum stress levels in the cycle: (a) 80%, (b) 75% and (c) 70% of σ_u. $\uparrow$ means no failure after 2 000 000 cycles. Bars indicate standard deviation.

is comparable (Fig. 4.16a) or higher than the unmodified material (material A) and the composite containing resin modified with only MFC (material D) (Fig. 4.16b). Decreasing the stress level (σ_{max} 70% of σ_u), i.e. in the high cycles regime, the combination of the two fillers generates a consistent reduction of fatigue life (see Figure 4.16c). For the lowest stress level, the best performance is of the composite D enhanced with the maximum of MFC. This does not fail after 2 000 000 cycles and shows a longer fatigue life than all the other composites including the unmodified one. The latter observation agrees with the results in [41].

The fatigue damage development in composite materials may be described by empirical metrics [64]. One of the main adopted damage metric is the stiffness degradation [65]. In the present fatigue investigation, the dynamic stiffness is selected as slope of segment passing through the points of maximum and minimum of the stress-strain cycle curve ("cycle stiffness"). Another damage metric, when instruments are not available for strain measurements, is the slope of the segment passing through the points of maximum and minimum stress-displacement cycle curve ("cycle slope") [61]. It should be noted that the cycle slope does not correspond to the cycle stiffness of the material because it has not been separated from the effects of compliance of the testing machine. In the following, the stiffness (measured with the extensometer or the digital image correlation) is adopted to have an overview of the damage development, but a comparison of the cycle slope and stiffness curved is first detailed. Diagrams in Figure 4.17, for three representative materials and three load levels, show very similar shape and, therefore, both metrics provide analogous qualitative information on the damage imparted during cyclic loading. This is valid for all the considered materials.

The influence of the imparted damage on the stiffness is presented, for

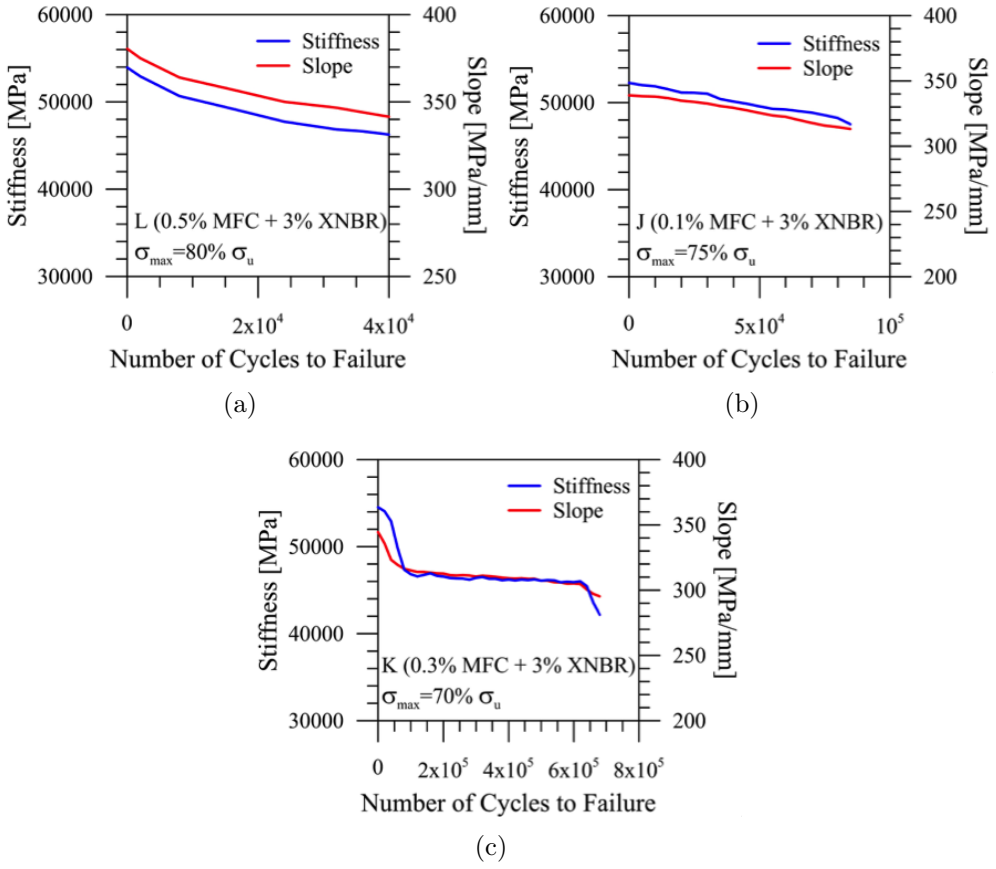

Figure 4.17: Comparison of the cycle slope and cycle stiffness for load levels: (a) 80% of σ_u material L, (b) 75% of σ_u material J and (c) 70% of σ_u material K.

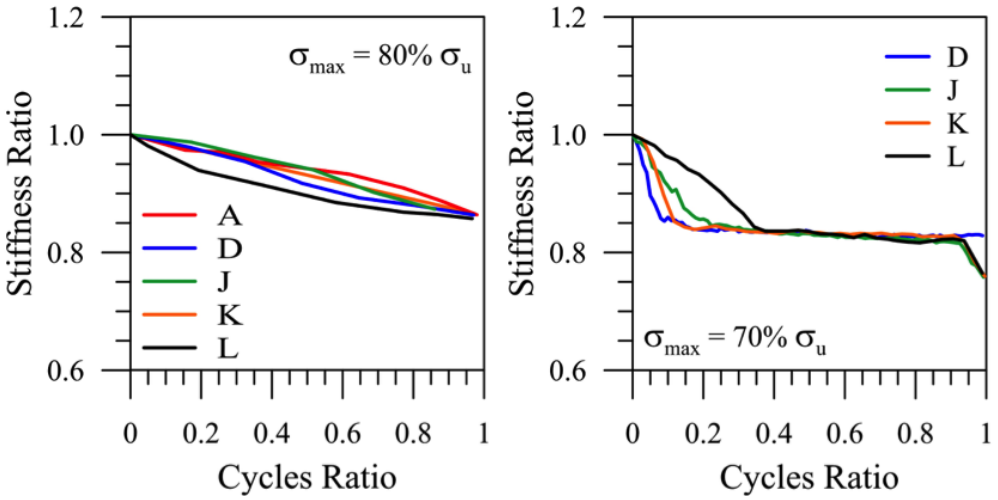

Figure 4.18: Stiffness ratio evolution for some specimens for two stress levels: (a) 80% and (b) 70% of σ_u.

sake of comparison, assuming the ratio of the cycle stiffness at the current cycle n and the initial stiffness (named "stiffness ratio"), and the fractional life [64] (named "cycles ratio") defined as the ratio n/N_f, being N_f the fatigue life. For highest cyclic stress level (i.e. 80% of σ_u), Figure 4.18a indicates a continuous almost linear degradation of the stiffness, a.k.a. a continuous developments of the damage in the composites leading to failure. This behavior is similar for all the hybrid modifications with an apparent initial faster stiffness decrease for material L, not significant being in the experimental scatter band. A similar trend was observed for specimens cyclic loaded with σ_{max} = 75% of σ_u. In the high cycles regime (i.e. 70% of σ_u), the diagram in Figure 4.18b highlights typical three stage curves [64] (curve of the material A is not included due to a problem in recording the signal of the extensometer). Initial stage with a rapid decrease of stiffness demonstrates a fast development of the damage until a fractional life of about 0.15. Material L, in the initial stage (Figure 4.18b), shows a lower slope of

the curve, meaning a slowest diffusion of damage in the material, reaching the same stiffness ratio (≈ 0.85) of the other materials in almost 35% of the fatigue life . In the second steady stage, the composites have a nearly linear low decrease of the stiffness until a fractional life of about 0.9. The third and final stage (Figure 4.18b) indicates a fast decrease of the stiffness of all materials as consequence of rapid spread of the damage until failure. This is not visible for specimens of material D that had no failure after 2 000 000 cycles.

4.4.1 DIC Measurements

The effects of cyclic loading can be judged considering the DIC analyses resulting in strain maps on the external surface of the central zone of the specimens. The high speed digital camera was adopted only for tests at the highest stress level (i.e. 80% of σ_u). The map of the strain component in the load direction for three different combination of fillers (D, J and L) and for the reference material (A) are depicted in Figure 4.19. The maps reproduce the strain distribution at the maximum stress in some cycles through the complete life of the specimens. Contours in Figure 4.19 show almost constant strain distribution except close to failure (maps in the right column). The strain component recorded on specimens A and J had maximum values up to failure in the same range of the quasi-static tensile tests ($0.012 \div 0.015$ see section 4.1), while materials D and L generate in the second half of the fatigue life a higher level of deformation. The latter and the longest fatigue life of composite D could be interpreted as a better damage tolerance of this material mainly related to a better fiber and matrix adhesion.

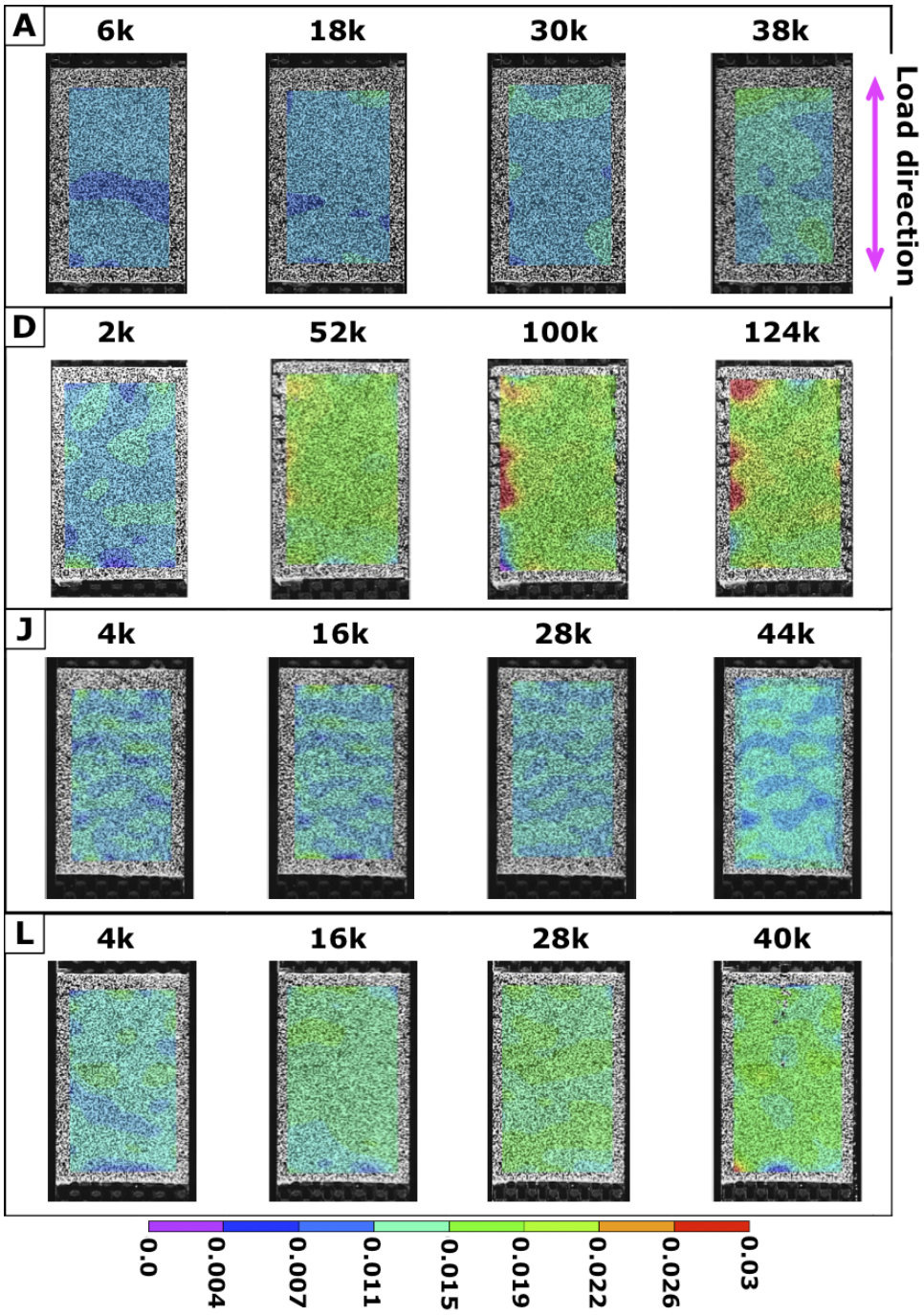

Figure 4.19: Maps of the strain component in the load direction at the maximum of the applied stress in the cycle, $\sigma_{max} = 80\%$ of σ_u, by DIC. From the top composite A, D, J and L.

4.4.2 SEM Observations

Scanning electron microscope (SEM) observations were performed on the fracture surface of specimens cyclically loaded with $\sigma_{max} = 75\%$ of σ_u. Images of Figure 4.20 refer to some combinations of MFC and XNBR content, i.e. composite A, D and J (see Table 2.7). Two main differences of the fracture surfaces are evident: the matrix deformation and the residual matrix on the fiber surface.

The fracture surface of the unmodified material (A) has relatively smooth and glassy epoxy matrix (see Figure 4.20a), typical of a brittle thermosetting polymer [66]. The adopted content of only MFC in composite D generates a clear extensive "plastic" deformation of the matrix (see Figure 4.20c). This is the first motivation for the longer fatigue life of the composite enhanced with MFC. The mix of MFC and XNBR increases the "plastic" deformation of the matrix with respect to the unmodified composite (A). In figure 4.20e is visible the rough matrix fracture surface for material J. This effect seems effective in extending the fatigue life in low cycle regime, but it is not for the high numbers of cycles as in material D (see Figure 4.16).

Observing the fracture surface at the fiber scale, the unmodified composite (A) shows very clean fibers, no residual resin is visible still in adhesion (see Figure 4.20b). The effect of MFC at fiber-matrix interface is clear in material D. The broken fibers had good adhesion to matrix (see Figure 4.20d), very few de-bondings were observed. This is the second motivation for the longer fatigue life of the composite with only MFC (D). For composites including both MFC and XNBR, the observed number of fiber-matrix de-bondings is remarkable (see Figure 4.20f) and, as consequence, the fatigue life is not improved or, for some contents and loading levels, a reduction was recorded.

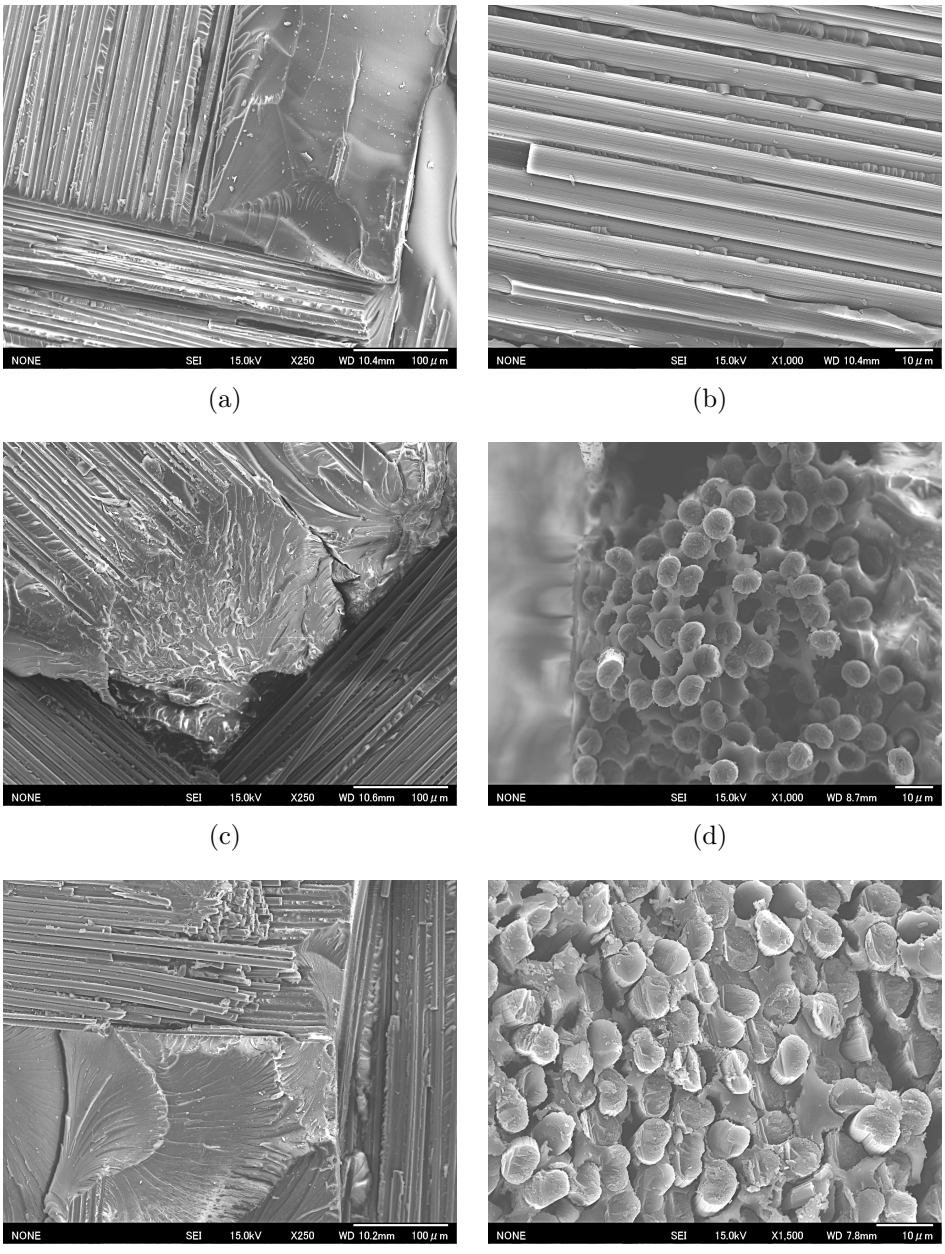

(a) (b)

(c) (d)

(e) (f)

Figure 4.20: SEM pictures after fatigue failure of specimens cyclically loaded with $\sigma_{max} = 80\%$ of σ_u. Composite (a-b) A, (c-d) D and (e-f) J.

Chapter 5

Conclusions and Future Developments

5.1 Conclusions

The results, presented in this study, show the effects of twelve different combinations of MFC and rubber contents in the epoxy resin (MFC in the range $0 \div 0.5$ wt% and XNBR $0 \div 3$ wt%) on the mechanical properties of composite laminates reinforced with carbon fibers plain weave fabrics. In the ranges of the adopted fillers content, the main results of the complete investigation are:

- The combination of MFC and XNBR does not provide relevant variations of the quasi-static tensile stiffness, while the tensile strength increases of about 10% for a mix of MFC in the range $0.1 \div 0.5$ wt% and 3 wt% of XNBR.

- The SEM images of the tensile damage modes show that the improvement of the mechanical properties depends on the fillers capacity to

enhance the adhesion between fiber and matrix as well as the matrix ductility.

- The main improvement of ILSS ($\approx +32\%$) was recorded with 0.1 wt% MFC and 3 wt% XNBR.

- The only important enhancement (more than 17%) of the Izod impact strength was observed for the composite containing 0.5 wt% of MFC (D).

- A reduction of fatigue life was observed for composites containing the hybrid matrix with higher contents of MFC and XNBR than that of the composites with only MFC.

- For the highest and lowest fatigue stress level, the best performance is of the composite enhanced with the maximum content of MFC. The combination of the two fillers generates a fatigue life almost similar to the unmodified material at the highest fatigue stress level and a consistent reduction of the fatigue life for the lowest stress level.

- The stiffness of the materials had similar degradation trend during the fatigue life, except the composite L (MFC 0.5 wt%, XNBR 3 wt%) with the lowest cyclic stress level, whose initial diffusion of the damage generates 85% of the initial stiffness in almost 35% of the fatigue life, while the others get the same reduction in the first 15% of the fatigue life.

- SEM observations of the fracture surface of specimens cyclically loaded with $\sigma_{max} = 80\%$ of σ_u indicate two main reasons for the better fatigue performance of material containing MFC (D): the extensive "plastic"

deformation of the matrix; the improved fibre and matrix adhesion up to the material failure.

As general conclusions, the hybridization of the epoxy resin with microfibrillated cellulose improves the fatigue and impact performances of the carbon plain weave composite. The highest contents of XNBR nanoparticles can reduce the fatigue life of the composites mainly in the high cycles regime, probably due to the effect of the increasing temperature during cyclic loading (see the preliminary monitoring of the temperature development during cyclic loading in Section 5.2).

The reliability of these conclusions, in term of fatigue life, can be assessed by the confidence level index, based on the Student's t-distribution [63]. The confidence levels in Table 5.1 show that: the hypothesis "the D composite has a longer fatigue life than the A" is valid with confidence level higher than 99% for all stress levels (the confidence level for 70% is not mentioned being the fatigue life of D longer than the other composites, material D does not fail after 2 million cycles); while, the hypothesis "the J composite has a longer fatigue life than the A" is valid with confidence level > 70%.

Stress level	**Confidence level**	
	D > A	J > A
[%] of σ_u	[%]	[%]
70	n.a.	73.04
75	99.96	99.98
80	99.11	70.63

Table 5.1: Confidence levels. > means longer fatigue life.

5.2 Future Developments

To further investigate the influence of the fillers on the fatigue performance of the considered composite materials, the damage nucleation and propagation can be monitored during tensile-tensile fatigue tests with other non destructive techniques.

An effective way to determine the damage progression in-situ is the thermography according to the literature ([67], [68], [69] and [70]). A preliminary thermal analysis was conducted in the present thesis and further investigations are suggested in future developments. Only four specimens in total were tested applying this technique.

5.2.1 Thermal Measurements

Thermography is a measurement technique which provides an image of the distribution of the temperature on the surface of the examined object. Thermography proceeds by decoding information "temperature" resulting from the infra-red radiation emitted by any object. The principal advantage of infra-red thermography is its non-intrusive character. Indeed, it forms part of the techniques of non-destructive testing and can be carried out on installations in service. The deformation of solid materials is almost always accompanied by releases of heat. When the material becomes deformed or is damaged, a part of energy necessary to starting and the propagation of the damage is transformed in an irreversible way into heat [71].

According to thermoelastic theory, the temperature of a material changes when the material changes volume due to mechanical work, and the temperature change can be related to the stress change in an adiabatic environment using Eq. 5.1 [72].

$$\Delta T = -\frac{T}{\rho C_p}(\alpha_{11}\Delta\sigma_1 + \alpha_{22}\Delta\sigma_2) \tag{5.1}$$

where, ΔT [K] is the temperature oscillation during a fatigue cycle on the surface of the specimen, T [K] is the absolute temperature on the surface of the specimen, ρ [kg^3/m] is the density, C_p [J K/kg] is the specific heat capacity at constant pressure, α_{11} and α_{22} [K^{-1}] are the surface coefficients of thermal expansion in 1 (warp) and 2 (weft) directions, and $\Delta\sigma_1$ and $\Delta\sigma_2$ are the amplitudes of the principal stresses at the surface ([70] and [72]).

Generally if the fatigue loading frequency is higher than 5 Hz, the loading process can be treated as adiabatic. Therefore the temperature difference between the peak and valley of the cyclic load can be related to the stress change, and the development of the stresses during the fatigue loading can be treated as an indicator of damage development.

The testing temperature was about 20 °C in this study and the variations also followed the change in room temperature. Therefore the temperature change between cycles was not used as an indicator of damage, instead the processed ΔT distribution between the peak and valley of a cycle was used to indicate fatigue damage [73]. Since the carbon fiber reinforcement and the matrix have different thermal expansion coefficients and are under different stress levels, the ΔT distribution also reflected the surface weave patterns. Similar phenomena have been observed in textile composites, which shows about 0.2 °C difference between the ΔT in the resin regions and in the tow regions ([70] and [74]). In order to distinguish and highlight the damage from the weave pattern, a ΔT_{var} distribution map was obtained by subtracting the first ΔT map (taken at 500 cycles) from all the other ΔT maps, to highlight the damage occurred after the initial recording.

For the maximum stress level (i.e. σ_{max} = 80% of σ_u), two specimens

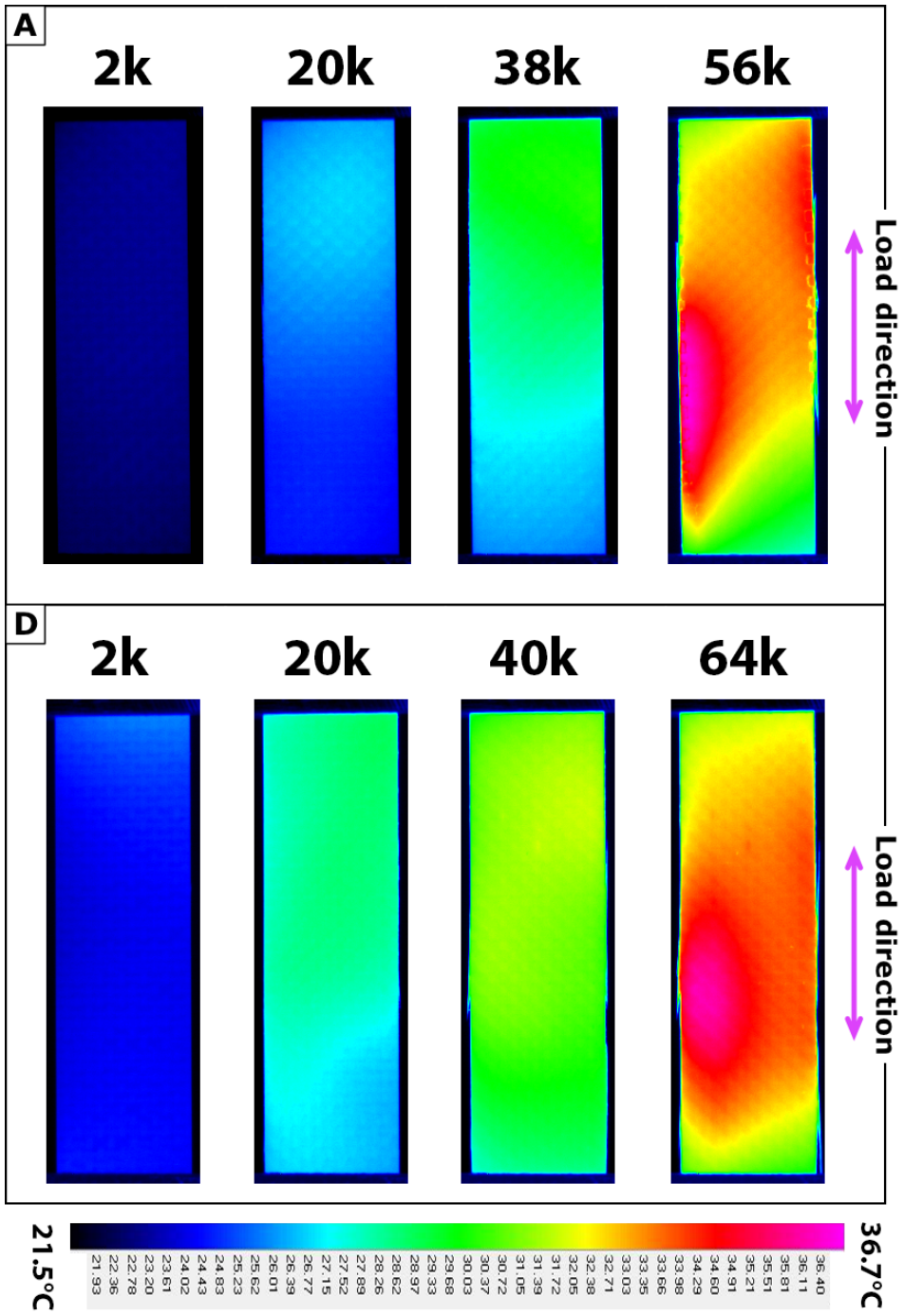

Figure 5.1: Temperature maps at the maximum of the applied stress in the cycle, σ_{max} = 80% of σ_u. Material A (top) and D (bottom).

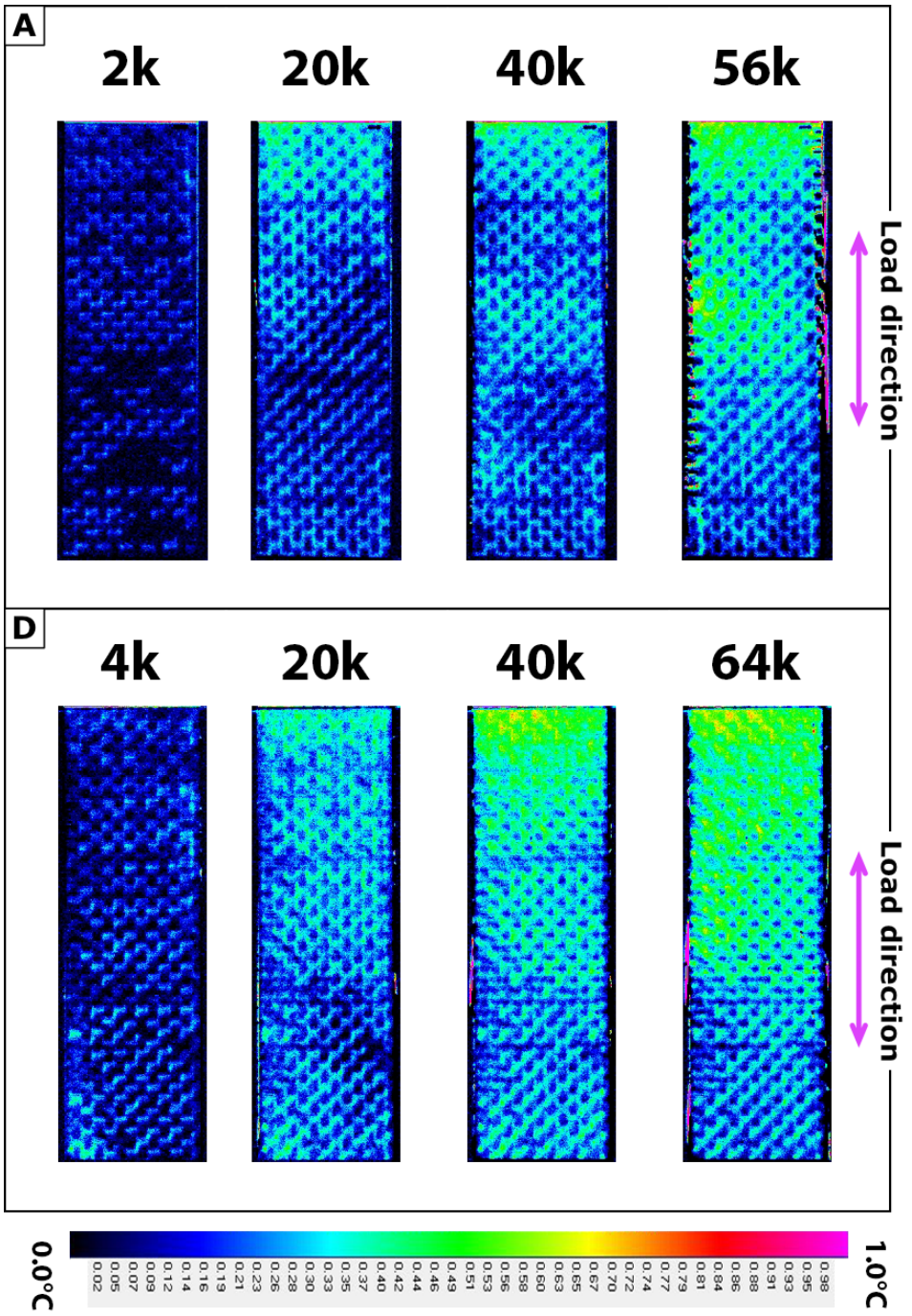

Figure 5.2: Variation of temperature amplitude with respect to first map (ΔT_{var}) for $\sigma_{max} = 80\%$ of σ_u. Material A (top) and D (bottom).

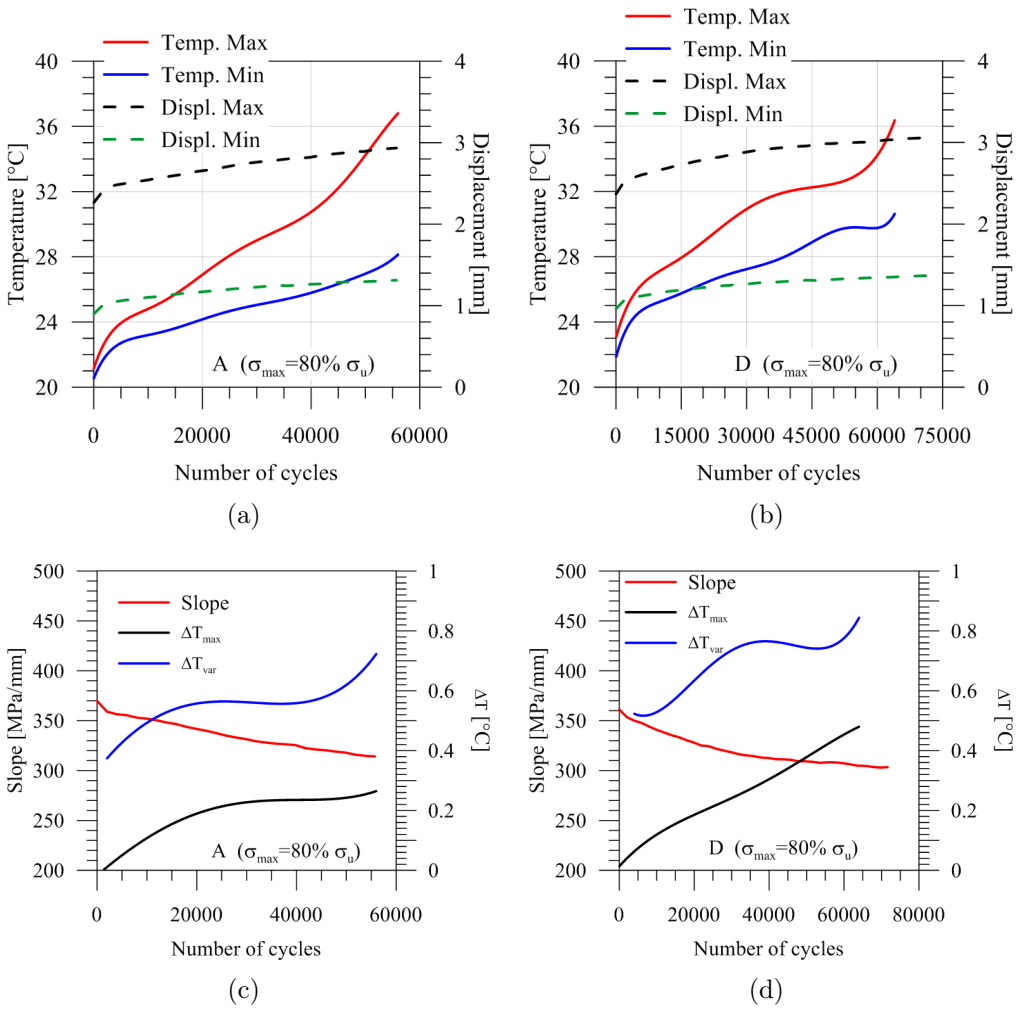

Figure 5.3: Maximum and minimum temperature and displacement vs. number of cycles for materials (a) A and (b) D. Slope, maximum temperature variation in the same cycle (ΔT_{max}) and difference with first map (ΔT_{var}) for materials (c) A and (d) D. $\sigma_{max} = 80\%$ of σ_u.

were tested: one of material A as a reference and one of material D containing 0.5 wt% of MFC. The two specimens showed a similar behavior,and a comparable fatigue life. Figure 5.1 and 5.2 show the temperature maps and the ΔT_{var} maps for different cycles, respectively.

The plots in Figure 5.3 represents the variation of the maximum and minimum temperature during the dynamic loading (Fig. 5.3a and 5.3b) and the temperature difference from peak to valley in cycle (ΔT_{max}) and the difference with the first map (ΔT_{var}) through the entire life of the specimens (Fig. 5.3c and 5.3d).

For the stress level of $\sigma_{max} = 75\%$ of σ_u, two specimens were tested: one of material A as a reference and one of material J containing 0.1 wt% of MFC and 3 wt% of XNBR. In this case, the two specimens showed a different behavior, see Figure 5.4 and 5.5 for the temperature maps and the ΔT_{var} maps, respectively. For the material A damage concentrates in the upper-left part, while for material J the progression of the damage is uniform until the failure.

The plots in Figure 5.6 represents the variation of the maximum and minimum temperature during the dynamic loading (Fig. 5.6a and 5.6b) and the temperature difference from peak to valley in cycle (ΔT_{max}) and the difference with the first map (ΔT_{var}) through the entire life of the specimens (Fig. 5.6c and 5.6d).

All the ΔT_{var} plots show a similar qualitative behavior which is also typical of the slope plots (reported in Fig. 5.3c-d and 5.6c-d): in a first phase the damage (i.e. ΔT_{var}) grows very fast in the specimens and reached a first local maximum, then in the second phase the ΔT_{var} (i.e. the damage) is almost constant and finally increases again up to the final failure.

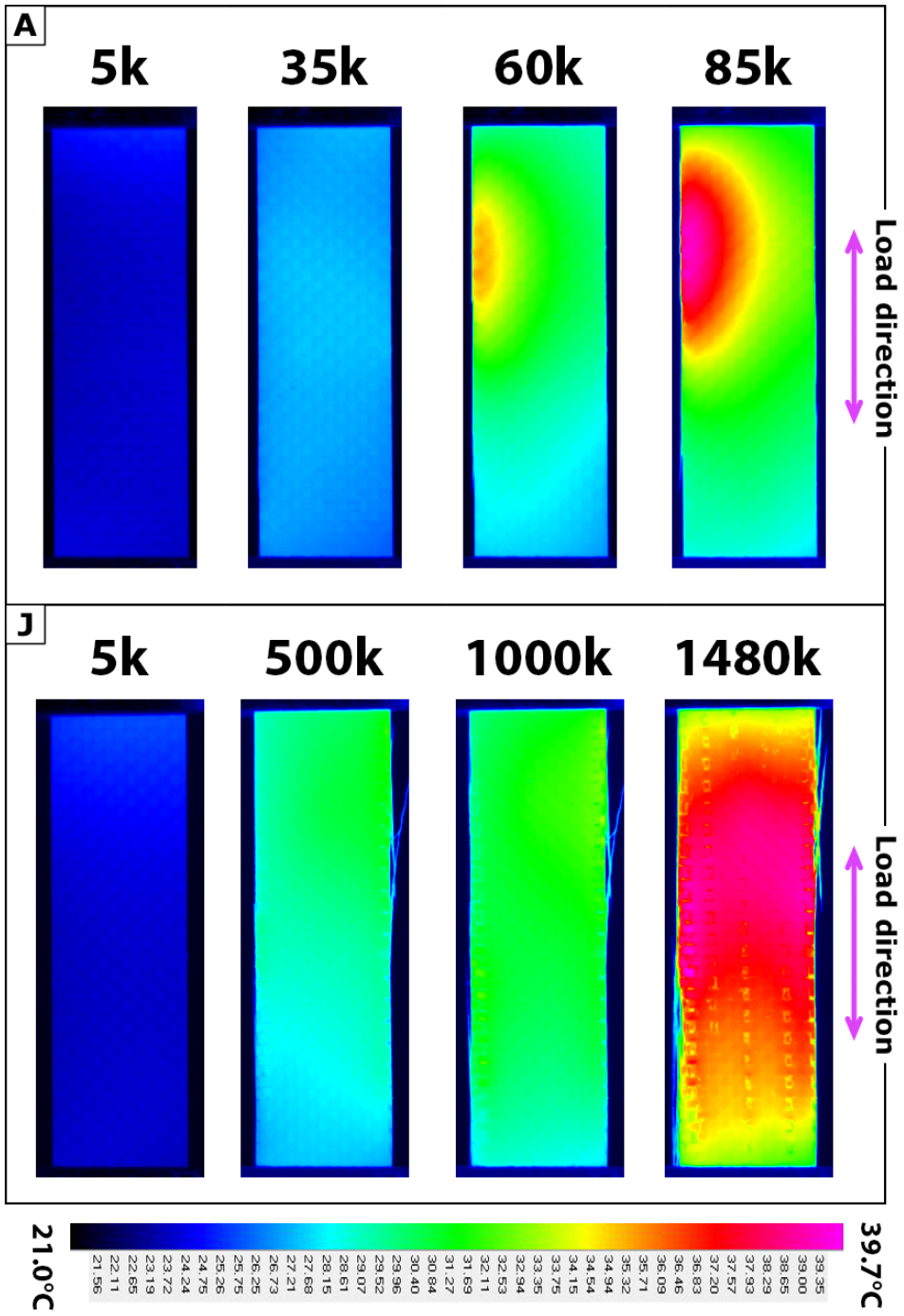

Figure 5.4: Temperature maps at the maximum of the applied stress in the cycle, $\sigma_{max} = 75\%$ of σ_u. Material A (top) and J (bottom).

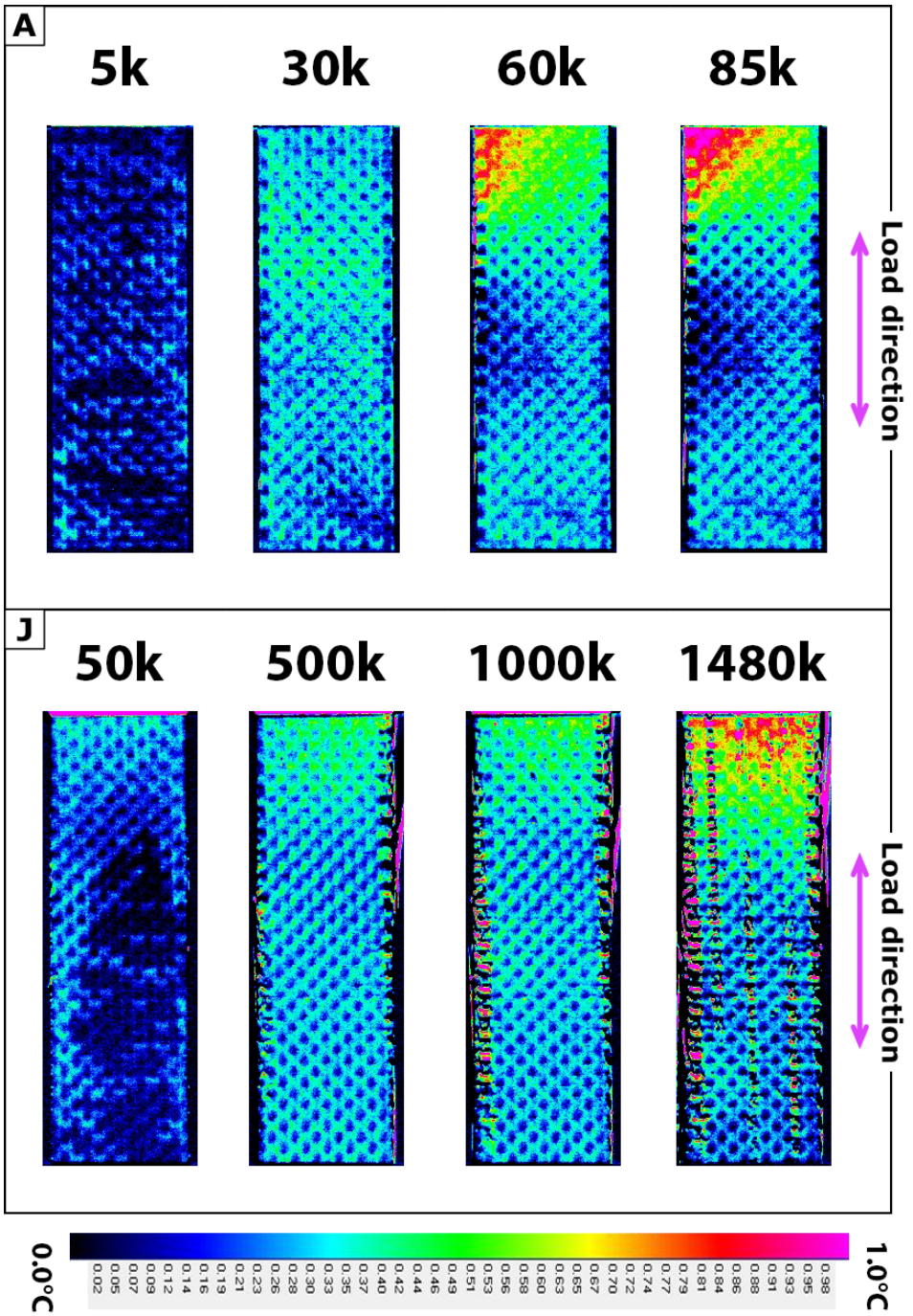

Figure 5.5: Variation of temperature amplitude with respect to first map for (ΔT_{var}) $\sigma_{max} = 75\%$ of σ_u. Material A (top) and J (bottom).

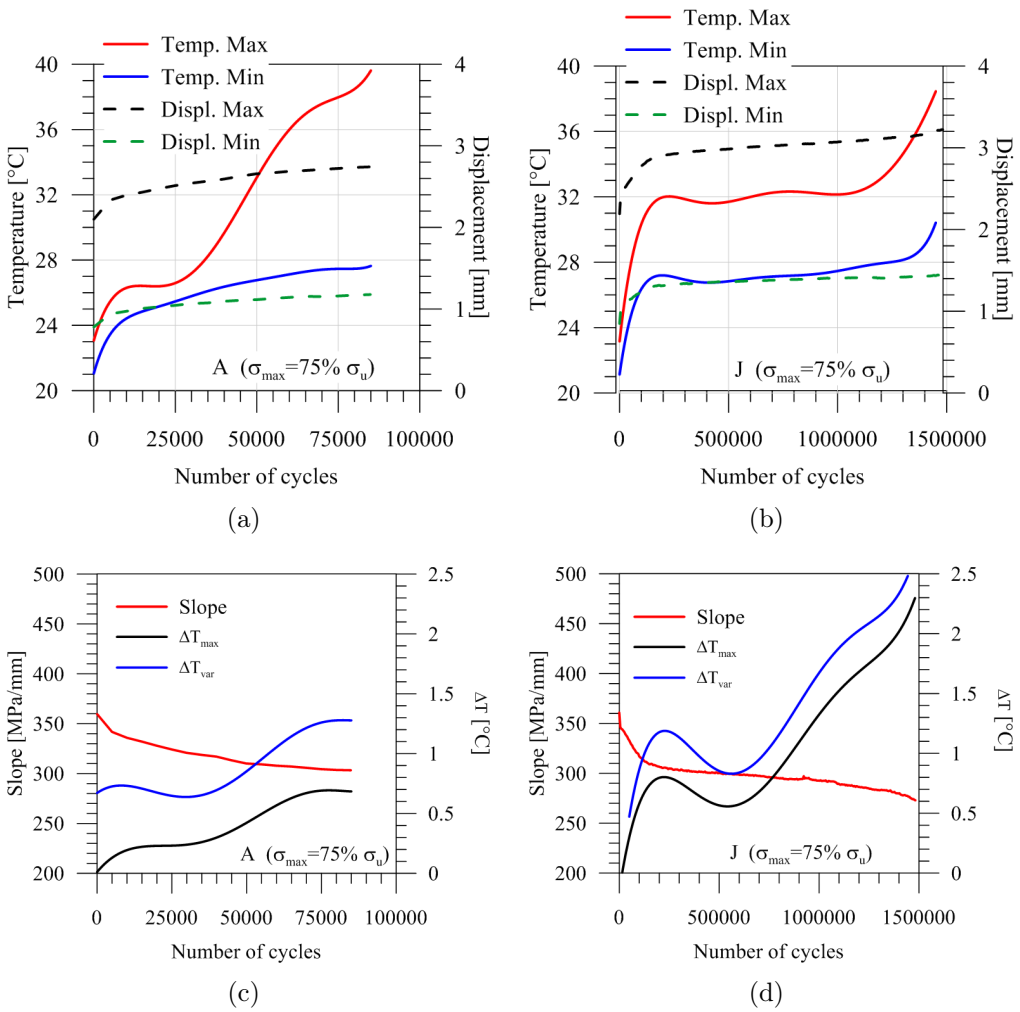

Figure 5.6: Maximum and minimum temperature and displacement vs. number of cycles for materials (a) A and (b) J. Slope, maximum temperature variation in the same cycle (ΔT_{max}) and difference with first map (ΔT_{var}) for materials (c) A and (d) J. $\sigma_{max} = 75\%$ of σ_u.

Bibliography

[1] D. R. Askeland, P. P. Fulay, and W. J. Wright, *The science and engineering of materials*, Sixth Edition. Stamford, CT, USA: Cengage Learning, 2006, isbn: 987-0-495-66802-2.

[2] D. Zenkert and M. Battley, *Mekanik, Foundations of fibre composites. Note for the course: Composite lightweight structures*. Denmark: T. U. of Denmark, Department of mechanical engineerign and DTU Mekanink, 2006.

[3] L. Tong, A. P. Mouritz, and M. Bannister, *3D Fibre Reinforced Polymer Composites*. Elsevier, Nov. 2002, isbn: 978-0-08-043938-9.

[4] J. Hale, "Boeing 787 from the ground up", vol. 10, 2010. [Online]. Available: `boeing.com/commercial/aeromagazine`.

[5] Y. Tang, L. Ye, Z. Zhang, and K. Friedrich, "Interlaminar fracture toughness and CAI strength of fibre-reinforced composites with nanoparticles – A review", *Composites Science and Technology*, vol. 86, pp. 26–37, Sep. 2013. doi: `10.1016/j.compscitech.2013.06.021`.

[6] A. E. Bogdanovich and M. H. Mohamed, "Three-dimensional reinforcements for composites", *SAMPE journal*, vol. 45, no. 6, pp. 8–28, 2009.

[7] A. P. Mouritz and B. N. Cox, "A mechanistic approach to the properties of stitched laminates", *Composites Part A: Applied Science and Manufacturing*, vol. 31, no. 1, pp. 1–27, 2000. DOI: 10.1016/S1359-835X(99)00056-1.

[8] S. V. Lomov, A. E. Bogdanovich, D. S. Ivanov, D. Mungalov, M. Karahan, and I. Verpoest, "A comparative study of tensile properties of non-crimp 3D orthogonal weave and multi-layer plain weave E-glass composites. Part 1: Materials, methods and principal results", *Composites Part A: Applied Science and Manufacturing*, vol. 40, no. 8, pp. 1134–1143, 2009. DOI: 10.1016/j.compositesa.2009.03.012.

[9] V. Carvelli, G. Gramellini, S. V. Lomov, A. E. Bogdanovich, D. D. Mungalov, and I. Verpoest, "Fatigue behavior of non-crimp 3D orthogonal weave and multi-layer plain weave E-glass reinforced composites", *Composites Science and Technology*, vol. 70, no. 14, pp. 2068–2076, 2010. DOI: 10.1016/j.compscitech.2010.08.002.

[10] M. H. G. Wichmann, J. Sumfleth, F. H. Gojny, M. Quaresimin, B. Fiedler, and K. Schulte, "Glass-fibre-reinforced composites with enhanced mechanical and electrical properties - Benefits and limitations of a nanoparticle modified matrix", *Engineering Fracture Mechanics*, vol. 73, no. 16, pp. 2346–2359, 2006. DOI: 10.1016/j.engfracmech.2006.05.015.

[11] M. Quaresimin and R. J. Varley, "Understanding the effect of nano-modifier addition upon the properties of fibre reinforced

laminates", *Composites Science and Technology*, vol. 68, no. 3-4, pp. 718–726, 2008. DOI: 10.1016/j.compscitech.2007.09.005.

[12] N. De Greef, L. Gorbatikh, A. Godara, L. Mezzo, S. V. Lomov, and I. Verpoest, "The effect of carbon nanotubes on the damage development in carbon fiber/epoxy composites", *Carbon*, vol. 49, no. 14, pp. 4650–4664, Nov. 2011. DOI: 10.1016/j.carbon.2011.06.047.

[13] L. Borrego, J. Costa, J. Ferreira, and H. Silva, "Fatigue behaviour of glass fibre reinforced epoxy composites enhanced with nanoparticles", *Composites Part B: Engineering*, vol. 62, pp. 65–72, 2014. DOI: 10.1016/j.compositesb.2014.02.016.

[14] S. Sprenger, "Fiber-reinforced composites based on epoxy resins modified with elastomers and surface-modified silica nanoparticles", *Journal of Materials Science*, vol. 49, no. 6, pp. 2391–2402, 2014. DOI: 10.1007/s10853-013-7963-8.

[15] Q. Zhao and S. V. Hoa, "Toughening Mechanism of Epoxy Resins with Micro/Nano Particles", *Journal of Composite Materials*, vol. 41, no. 2, pp. 201–219, 2006. DOI: 10.1177/0021998306063361.

[16] A. F. Turbak, F. W. Snyder, and K. R. Sandberg, "Suspensions Containing Microfibrillated Cellulose", pp. 4–7, Feb. 19–19, 1985.

[17] M. Darder, P. Aranda, and E. Ruiz-Hitzky, "Bionanocomposites: A New Concept of Ecological, Bioinspired, and Functional Hybrid Materials", *Advanced Materials*, vol. 19, no. 10, pp. 1309–1319, May 2007. DOI: 10.1002/adma.200602328.

[18] A. K. Bledzki and J. Gassan, "Composites reinforced with cellulose based fibres", *Progress in Polymer Science*, vol. 24, pp. 221–274, 1999.

[19] F. W. Herrick, R. L. Casebier, K. J. Hamilton, and K. R. Sandberg, "Microfibrillated Cellulose: Morphology and Accessibility", *Journal of Applied Polymer Science: Applied Polymer Symposium*, vol. 37, pp. 797–813, CONF-8205234-Vol.2 1983.

[20] N. Lavoine, I. Desloges, A. Dufresne, and J. Bras, "Microfibrillated cellulose – Its barrier properties and applications in cellulosic materials: A review", *Carbohydrate Polymers*, vol. 90, no. 2, pp. 735–764, 2012. DOI: 10.1016/j.carbpol.2012.05.026.

[21] N. Soykeabkaew, N. Arimoto, T. Nishino, and T. Peijs, "All-cellulose composites by surface selective dissolution of aligned ligno-cellulosic fibres", *Composites Science and Technology*, vol. 68, no. 10-11, pp. 2201–2207, Aug. 2008. DOI: 10.1016/j.compscitech.2008.03.023.

[22] M. H. Gabr, M. A. Elrahman, K. Okubo, and T. Fujii, "Effect of microfibrillated cellulose on mechanical properties of plain-woven CFRP reinforced epoxy", *Composite Structures*, vol. 92, no. 9, pp. 1999–2006, 2010. DOI: 10.1016/j.compstruct.2009.12.009.

[23] R. A. Pearson and A. F. Yee, "Toughening mechanisms in elastomer-modified epoxies - Part 3 The effect of cross-link density", *Journal of Materials Science*, vol. 24, no. 7, pp. 2571–2580, 1989. DOI: 10.1007/BF01174528.

[24] Y. Zhao, Z.-K. Chen, Y. Liu, H.-M. Xiao, Q.-P. Feng, and S.-Y. Fu, "Simultaneously enhanced cryogenic tensile strength and

fracture toughness of epoxy resins by carboxylic nitrile-butadiene nano-rubber", *Composites Part A: Applied Science and Manufacturing*, vol. 55, pp. 178–187, Dec. 2013. DOI: 10.1016/j.compositesa.2013.09.005.

[25] A. Kinloch, S. Lee, and A. Taylor, "Improving the fracture toughness and the cyclic-fatigue resistance of epoxy-polymer blends", *Polymer*, vol. 55, no. 24, pp. 6325–6334, 2014. DOI: 10.1016/j.polymer.2014.10.018.

[26] C. M. Manjunatha, a. C. Taylor, a. J. Kinloch, and S. Sprenger, "The cyclic-fatigue behaviour of an epoxy polymer modified with micron-rubber and nano-silica particles", *Journal of Materials Science*, vol. 44, no. 16, pp. 4487–4490, Jun. 2009. DOI: 10.1007/s10853-009-3653-y.

[27] H.-Y. Liu, G. Wang, and Y.-W. Mai, "Cyclic fatigue crack propagation of nanoparticle modified epoxy", *Composites Science and Technology*, vol. 72, no. 13, pp. 1530–1538, Aug. 2012. DOI: 10.1016/j.compscitech.2012.05.025.

[28] N. G. Ozdemir, T. Zhang, H. Hadavinia, I. Aspin, and F. Scarpa, "Influence of nanorubber toughening on the tensile deformation and tensile fatigue behaviour of a carbon fibre-reinforced epoxy composite", *Journal of Composite Materials*, 2015. DOI: 10.1177/0021998315609976.

[29] A. F. Yee and R. A. Pearson, "Toughening mechanisms in elastomer-modified epoxies - Part 1 Mechanical studies", *Journal of Materials Science*, vol. 21, no. 7, pp. 2462–2474, 1986. DOI: 10.1007/BF01114293.

[30] M. H. Gabr, M. A. Elrahman, K. Okubo, and T. Fujii, "Interfacial adhesion improvement of plain woven carbon fiber reinforced epoxy filled with micro-fibrillated cellulose by addition liquid rubber", *Journal of Materials Science*, vol. 45, no. 14, pp. 3841–3850, Apr. 2010. DOI: 10.1007/s10853-010-4439-y.

[31] M. H. Gabr, M. A. Elrahman, K. Okubo, and T. Fujii, "A study on mechanical properties of bacterial cellulose/epoxy reinforced by plain woven carbon fiber modified with liquid rubber", *Composites Part A: Applied Science and Manufacturing*, vol. 41, no. 9, pp. 1263–1271, 2010. DOI: 10.1016/j.compositesa.2010.05.010.

[32] Mitsubishi Co. Ltd., *Curing Angent / Chemical Property*, 2012. [Online]. Available: http://www.m-kagaku.co.jp/english/products/business/function/specialty2/details/__icsFiles/afieldfile/2013/11/05/CuringAgentCatalogue_1_MCC.pdf (visited on 19/10/2015).

[33] Mitsubishi Co. Ltd., *Epoxy Resin - Products and services*, 2012. [Online]. Available: http://www.m-kagaku.co.jp/english/products/business/function/specialty2/details/1194653_3409.html (visited on 19/10/2015).

[34] Mitsubishi Co. Ltd., *General Grade Catalogue*, 2012. [Online]. Available: http://www.m-kagaku.co.jp/english/products/business/function/specialty2/details/__icsFiles/afieldfile/2013/11/05/GeneralGradeCatalogue_EX_MCC.pdf (visited on 19/10/2015).

[35] Mitsubishi Rayon Co. Ltd., *Pyrofil Product List*, Jan.–2013. [Online]. Available: https://www.mrc.co.jp/pyrofil/english/product/pdf/cf.pdf (visited on 21/10/2015).

[36] Mitsubishi Rayon Co. Ltd., *Pyrofil Typical Properties of Carbon Fibers*, Nov.–2013. [Online]. Available: https://www.mrc.co.jp/pyrofil/english/product/pdf/cf.pdf (visited on 21/10/2015).

[37] A. B. Mabrouk, H. Kaddami, S. Boufi, F. Erchiqui, and A. Dufresne, "Cellulosic nanoparticles from alfa fibers (Stipa tenacissima): Extraction procedures and reinforcement potential in polymer nanocomposites", *Cellulose*, vol. 19, no. 3, pp. 843–853, Feb. 2012. doi: 10.1007/s10570-012-9662-z.

[38] Daicel Chemical Industries Ltd., *CELISH / TIARA (Microfibrillated products)*. [Online]. Available: http://www.daicelfinechem.jp/en/business/wspdiv/celish.html (visited on 20/10/2015).

[39] F. Van Beurden, *XNBR strings with Carboxylgroups and Zinc++ ionic links along the sulfur bridges of the vulcanisation*, 13 5, 2012. [Online]. Available: https://commons.wikimedia.org/wiki/File:XNBR_extended_structure.jpg (visited on 10/20/2015).

[40] JSR Corporation Ltd., *Acrylonitrile-Butadiene Rubber*. [Online]. Available: http://www.jsr.co.jp/jsr_e/pdf/pd/el/JSRNBR_e.pdf (visited on 20/10/2015).

[41] N. Takagaki, K. Okubo, and T. Fujii, "Improvement of fatigue strength and impact properties of plain-woven CFRP modified with

Micro Fibrillated Cellulose", *Advanced Materials Research*, vol. 47-50, pp. 133–136, 2008.

[42] European commitee for standardization, *EN ISO 1172 Textile glass reinforced plastics, prepreg moulding compounds and laminates. Determination of the textile-glass and mineral-filler content - Calcination Methods*, Aug. 1998.

[43] Kett Electric Laboratory, *Infrared Moisture Determination Balance FD-720*. [Online]. Available: `http://www.kett.co.jp/english/products/c_3/7.html` (visited on 29/10/2015).

[44] ASTM International, *D3039 Standard test method for tensile properties of polymer matrix composite materials*, 2008.

[45] ASTM International, *D2344 Standard test method for short-beam strength of polymer matrix composite materials and their laminates*, 2006.

[46] Japanese Industrial Standard, *JIS K 7062 Testing Methods of Izod impact strength of glass fiber reinforced plastics*, 1992.

[47] Shimadzu Corporation, *Autograph AG-IS Series*. [Online]. Available: `http://www.ssi.shimadzu.com/products/literature/testing/agis.pdf` (visited on 29/10/2015).

[48] Kyowa Electronic Instruments Co., Ltd., *PCD-300 Series Sensor Interfaces*. [Online]. Available: `http://www.kyowa-ei.com/eng/download/support/download/catalog/s_pcd-300_series_catalog_1402_01_eng.pdf` (visited on 30/10/2015).

[49] Kyowa Electronic Instruments Co., Ltd., *DCS-100A series Dynamic data acquisition software*. [Online]. Available: http://www.kyowa-ei.com/eng/product/category/software/s_dcs-100a_series/index.html (visited on 30/10/2015).

[50] ASTM International, *D3479 Standard test method for tension-tension fatigue of polymer matrix composite materials*, 2012.

[51] Shimadzu Corporation, *Servopulser Fatigue and Endurance Testing Systems*. [Online]. Available: http://www.ssi.shimadzu.com/products/literature/testing/shimadzu_servopulser_brochure.pdf (visited on 30/10/2015).

[52] nac Image Technology Inc., *NAC's Memrecam fx K3 and K3R Digital High- Speed Color Video System*. [Online]. Available: http://www.couriertronics.com/docs/NAC_Documents/Memrecam_fx_K3_K3R_Specification_Sheet.pdf (visited on 03/11/2015).

[53] Correlated Solutions, Inc., *The VIC-2D^{TM} System*. [Online]. Available: http://www.correlatedsolutions.com/vic-2d/ (visited on 05/11/2015).

[54] FLIR Systems, Inc., *FLIR SC7000 Series*. [Online]. Available: http://www.flirmedia.com/MMC/THG/Brochures/RND_017/RND_017_US.pdf (visited on 05/11/2015).

[55] Keyence Corporation, *Microscope VHX-2000 series*. [Online]. Available: http://www.keyence.com/products/microscope/digital-microscope/vhx-2000/features/index.jsp (visited on 05/11/2015).

[56] KEYENCE CORPORATION, *VH-Z100R Wide-range Zoom Lens (100-1000X)*. [Online]. Available: http://www.keyence.com/products/microscope/digital-microscope/vh_lens/models/vh-z100r/index.jsp (visited on 05/11/2015).

[57] JEOL LTD., *JSM-7001F Schottky Emission Scanning Electron Microscope*. [Online]. Available: http://www.jeol.co.jp/en/products/detail/JSM-7001F.html (visited on 05/11/2015).

[58] G. J. CURTIS, J. M. MILNE, and W. N. REYNOLDS, "Non-hookean behaviour of strong carbon fibers", *Nature*, vol. 220, pp. 1024–1025, Dec. 1968. DOI: 10.1038/2201024a0.

[59] M. SHIOYA, E. HAYAKAWA, and a. TAKAKU, "Non-hookean stress-strain response and changes in crystallite orientation of carbon fibres", *Journal of Materials Science*, vol. 31, no. 17, pp. 4521–4532, 1996. DOI: 10.1007/BF00366347.

[60] N. TOYAMA and J. TAKATSUBO, "An investigation of non-linear elastic behavior of CFRP laminates and strain measurement using Lamb waves", *Composites Science and Technology*, vol. 64, pp. 2509–2516, 2004. DOI: 10.1016/j.compscitech.2004.05.007.

[61] V. CARVELLI, J. PAZMINO, S. V. LOMOV, A. E. BOGDANOVICH, D. D. MUNGALOV, and I. VERPOEST, "Quasi-static and fatigue tensile behavior of a 3D rotary braided carbon/epoxy composite.", *Journal of Composite Materials*, vol. 47, no. 25, pp. 3195–3209, 2013. DOI: 10.1177/0021998312463407.

[62] F. H. Chowdhury, M. V. Hosur, and S. Jeelani, "Studies on the flexural and thermomechanical properties of woven carbon/nanoclay-epoxy laminates", *Materials Science and Engineering A*, vol. 421, pp. 298–306, 2006. doi: 10.1016/j.msea.2006.01.074.

[63] L. J. Bain and M. Engelhardt, *Introduction to probability and mathematical statistics*, 2nd, ser. Duxbury Classic. Duxbury Press, Mar. 17, 2000, 656 pp., isbn: 978-0-534-38020-5.

[64] A. Gagel, B. Fiedler, and K. Schulte, "On modelling the mechanical degradation of fatigue loaded glass-fibre non-crimp fabric reinforced epoxy laminates", *Composites Science and Technology*, vol. 66, no. 5, pp. 657–664, May 2006. doi: 10.1016/j.compscitech.2005.07.037.

[65] M. Gude, W. Hufenbach, and I. Koch, "Damage evolution of novel 3D textile-reinforced composites under fatigue loading conditions", *Composites Science and Technology*, vol. 70, no. 1, pp. 186–192, 2010. doi: 10.1016/j.compscitech.2009.10.010.

[66] T. H. Hsieh, A. J. Kinloch, K. Masania, J. Sohn Lee, A. C. Taylor, and S. Sprenger, "The toughness of epoxy polymers and fibre composites modified with rubber microparticles and silica nanoparticles", *Journal of Materials Science*, vol. 45, no. 5, pp. 1193–1210, Dec. 2009. doi: 10.1007/s10853-009-4064-9.

[67] G. La Rosa, C. Clienti, and F. Lo Savio, "Fatigue analysis by acoustic emission and thermographic techniques", *Procedia Engineering*, vol. 74, pp. 261–268, 2014. doi: 10.1016/j.proeng.2014.06.259.

[68] J. Cuadra, P. a. Vanniamparambil, K. Hazeli, I. Bartoli, and A. Kontsos, "Damage quantification in polymer composites using a hybrid NDT approach", *Composites Science and Technology*, vol. 83, pp. 11–21, 2013. doi: 10.1016/j.compscitech.2013.04.013.

[69] D. S. de Vasconcellos, F. Touchard, and L. Chocinski-Arnault, "Tension–tension fatigue behaviour of woven hemp fibre reinforced epoxy composite: A multi-instrumented damage analysis", *International Journal of Fatigue*, vol. 59, pp. 159–169, 2014. doi: 10.1016/j.ijfatigue.2013.08.029.

[70] R. K. Fruehmann, J. M. Dulieu-Barton, and S. Quinn, "Assessment of fatigue damage evolution in woven composite materials using infra-red techniques", *Composites Science and Technology*, vol. 70, no. 6, pp. 937–946, 2010. doi: 10.1016/j.compscitech.2010.02.009.

[71] A. Chrysochoos, "Infrared thermography, a potential tool for analysing the material behaviour", *Mecanique & Industries*, vol. 3, no. 1, pp. 3–14, 2002.

[72] P. Stanley and W. K. Chan, "The application of thermoelastic stress analysis techniques to composite materials", *The Journal of Strain Analysis for Engineering Design*, vol. 23, no. 3, pp. 137–143, 1988.

[73] S. Dai, P. Cunningham, S. Marshall, and C. Silva, "Open hole quasi-static and fatigue characterisation of 3D woven composites", *Composite Structures*, vol. 131, pp. 765–774, 2015. doi: 10.1016/j.compstruct.2015.06.032.

[74] R. Fruehmann, J. Dulieu-Barton, and S. Quinn, "On the thermoelastic response of woven composite materials", *The Journal of Strain Analysis for Engineering Design*, vol. 43, no. 6, pp. 435–450, 2008, issn: 0309-3247.

Acknowledgments

First of all, I would like to thank Prof. Toru Fujii and Prof. Valter Carvelli, for giving me the possibility to carry out my master thesis at Doshisha University, supervising the experimental activities and providing helpful suggestions throughout the entire project.

The support of Japan Society for the Promotion of Science, KAKENHI Grant Number 26289012, is gratefully acknowledged.

Thanks to Dr. Yongzheng Shao, Dr. Phong Nguyen Tien and Dr. Mohamed Gabr Hassan Radwan for their constant help, they introduced me to the experimental activities in Doshisha.

Of course, my most sincere thanks go to my friend Gibeop Nam, who always offered me a great support and contributed to make my experience in Japan unforgettable.

I would like to thank every member of the Advanced Material and Structural Engineering Laboratory, AMSEL, especially Maehata, Ooka and Hieda, for their constant help and availability.

The greatest acknowledgment goes to my parents Paola and Giancarlo, and to my sister Silvia: they always believed in me and offered their support throughout my academic career.

A special thank to Glenda, for her constant encouragement during my stay in Japan.

Finally, thank you to all my friends and my classmates, for their companionship in my academic years.

List of Publications

A. Betti, V. Carvelli, T. Fujii, and K. Okubo, "Hybrid Modification of Epoxy Resin with Micro-Fibrillated Cellulose and Rubber Nanoparticle: Effects on the Mechanical Properties of Carbon Plain-Weave Reinforced Composites", *International Journal of Aerospace and Lightweight Structures*, vol. 03, no. 04, pp. 473–486, 2013. doi: 10.3850/S2010428614000038.

N. T. Phong, M. H. Gabr, V. M. Duc, A. Betti, K. Okubo, B. Chuong, and T. Fujii, "Improved fracture toughness and fatigue life of carbon fiber reinforced epoxy composite due to incorporation of rubber nanoparticles", *Journal of Materials Science*, vol. 48, no. 17, pp. 6039–6047, 2013, issn: 0022-2461.

V. Carvelli, A. Betti, and T. Fujii, "Fatigue and Izod impact performance of carbon plain weave textile reinforced epoxy modified with cellulose microfibrils and rubber nanoparticles", *Composites Part A: Applied Science and Manufacturing*, Submitted, 2015.